Final Master's Thesis

Mimic cell membranes. Thermodynamic and Atomic Force Microscopy studies

Author

Laura Dotor Delgado

Supervisors

Dr. Pilar Cea Mingueza and Dr. Santiago Martín Soláns

Universidad de Zaragoza
2020-2021

Table of contents

Abstract

Mimic cell membranes are crucial for the understanding of cellular processes since the biological membrane is too complex to be deeply studied *in vivo*. In this Master's Project, dipalmitoylphosphatidylcholine (DPPC) and cholesterol (CHOL) constitute the model cell membrane in order to study their interaction with curcumin (CCM). In the last decades, this xenobiotic has become a relevant compound in encapsulated cell therapy and clinical trials because it exhibits anti-cancer, antioxidant, neuroprotector, antidepressant and anti-inflammatory effects. Consequently, a comprehensive study at the air-water interface of single, binary and ternary monolayers was performed by means of the Langmuir technique. The thermodynamic results are indicative of a partial miscibility between the components. In general, the miscibility increases as the monolayer is more condensed and, depending on the composition, the monolayers show more expanded phases as compared to those of the pure compounds. For both CCM-DPPC and CCM-CHOL binary monolayers, the most favourable mixture in terms of the steric and energetic effects is $x_{CCM} = 0.8$. On the other hand, for the DPPC-CHOL binary monolayers, the most favourable mixture is $x_{DPPC} = 0.6$. With respect to the ternary monolayers, the most favourable mixtures are $x_{CCM} = 0.2$ and 0.4; it must be taken into account that the Eucaryotic cells contain DPPC-CHOL 1:1 and that the biological surface pressure is about 30 $mN \cdot m^{-1}$. Finally, selected Langmuir-Blodgett films were inspected by Atomic Force Microscopy (AFM); the morphology of the images supports the conclusion of partial miscibility of the components as deduced from the thermodynamic study.

1 Objectives

The first objective of this Master's Thesis is to provide the student with competences at the Master's level and with a high level of specialization in a chosen topic in the field of Nanotechnology. Therefore, the main academic objectives are: to apply theoretical knowledge learned in the different modules of the Master's Degree through a multidisciplinary approach, to work independently in the laboratory and to extract critical conclusions from the experimental results aided by a rigorous literature search. Additionally, the collaborative work with other master and Ph-D students as well as postdoc and senior researchers is expected to provide the student with key scientific and transversal competences; for instance, teamwork and a realistic approach about the *status quo* of a researcher. Furthermore, communication skills are assessed through this written document and the oral presentation of the results to a panel of examiners.

On the other hand, the scientific objective of this Master's Thesis is to enlarge the understanding of the molecular interactions within the components of a model cell membrane (phospholipids and cholesterol) with a xenobiotic (curcumin). Consequently, a comprehensive study at the air-water interface of single, binary and ternary monolayers was performed by means of the Langmuir technique, and thermodynamic parameters such as the thermodynamic excess area of mixing, the Gibbs surface excess energy of mixing, the Gibbs energy of mixing and the Young modulus were calculated. In addition, Langmuir-Blodgett films of selected monolayers were characterized by Atomic Force Microscopy in order to study the topography and provide additional information about the miscibility of the components.

2 Introduction

We must not let our desires for a specific result cloud our perceptions. […]
But how can we not, in searching, wish for a specific result?
What scientist goes into a project without a hope for what they will find?
—*Rhythm of War* (Book 4 of *The Stormlight Archives*), Brandon Sanderson

Curcumin (CCM) is a relevant compound in pharmaceutical applications due its low toxicity and anti-cancer, antioxidant, neuroprotector, antimicrobial, antidepressant and anti-inflammatory effects.[1–4] It is the major compound (77%) of turmeric (*Curcuma longa)* which is a flowering plant of the ginger family *Zingiberaceae*; the other main compounds are demethoxycurcumin (18%) and bisdemethoxycurcumin (5%). Turmeric was registered for the first time in the book *Xin xiu ben cao* (659 a.C.)[5] and it has been employed as traditional medicine and natural dye. Also, it is the main ingredient of curry. The curcumin compound was isolated for the first time in 1815; its chemical structure is shown in **Figure 2-1** and the chemical and physical properties are further described in **ANNEX I**.[6]

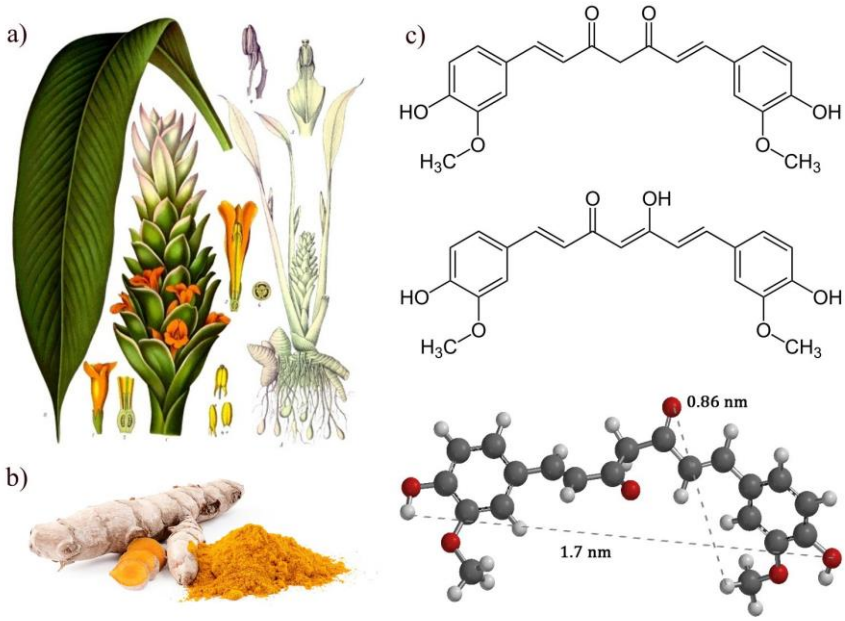

Figure 2-1. a) Botanical view of *Curcuma longa.* b) Turmeric rhizome and powder. Credit: Simon A. Eugster CC BY-SA 3.0. c) Chemical structure of curcumin (up) ceto (center) enol (down) ceto representation with Spartan Software.

Unfortunately, its low bioavailability hampers the use of curcumin as therapeutic agent; in a rat study, oral administration of a single dose of 2 g resulted in plasma concentration of less than 5 $\mu g \cdot mL^{-1}$ indicating that curcumin displays poor absorption

into the gastrointestinal tract[7], which can be related with its low solubility in the aqueous media. As a result, the interactions of curcumin with biological cell membranes must be further studied.

Cell membranes are crucial to the life of the cell. The plasma membrane encloses the cell and defines the boundaries between the cytosol and the extracellular environment. Moreover, inside eukaryotic cells, the membranes of the nucleus and membrane-enclosed organelles maintain the characteristic differences between the contents of each organelle and the cytosol. In spite of their differing functions, all biological membranes have a common general structure: a lipid bilayer about 5 nm thick, in which protein molecules are embedded and held together mainly by noncovalent interactions. Phosphoglycerides, sphingolipids and sterols are the major lipids in cell membranes. In particular, Eukaryotic plasma membranes contain up to one molecule of cholesterol for every phospholipid molecule; although cholesterol tightens the packing of the lipids in a bilayer, it does not make membranes any less fluid. Furthermore, glycolipids such as gangliosides are found on the surface of all Eukaryotic plasma membranes. Despite their fluidity, lipid bilayers can form phase segregations in which specific lipids come together in separate domains, known as lipid rafts. In addition, lipid molecules can move in the bilayer by lateral diffusion, flexion, rotation and flip-flop motion. Regarding the membrane proteins, the amounts and types are highly variable; typical plasma membrane presents protein accounting for about half of its mass. Summarizing, biological membranes are asymmetric, dynamic and fluid structures.[8]

The molecules that are not produced by the organism are namely xenobiotics (derived from the Greek words ξένο 'stranger' y βιο 'life') ant their origins can be both natural and artificial. The magnitude of the effect of a xenobiotic in an organism depends on the concentration of the active compound in the target, so the effect is limited by the bioavailability of the compound and its transport across barriers; apart from its structural function, the lipid bilayer serves as a relatively permeable barrier to the passage of hydrophobic molecules, while membrane proteins transport hydrophilic and more specific molecules across it. However, due to the high complexity of biological membranes, studies *in vivo* are quite difficult to perform. Consequently, cell membrane models are usually proposed;[9] in terms of the fabrication method, the most

common systems include the rupture of lipid vesicles and supported lipid monolayers and bilayers deposited by Langmuir-Blodgett or Langmuir-Schaefer methodologies.[10]

In this Master's Thesis dipalmitoylphosphatidylcholine (DPPC) and cholesterol (CHOL) are selected to form the mimic cell membrane. On the one hand, DPPC constitutes the main component of biological membranes, in particular it is the major component in the membranes of lung cells and it presents neutral charge and high stability.[11] On the other hand, CHOL is a key molecule in the composition of membranes because it modules the fluidity and the asymmetry of the bilayer.[12] The chemical structures of DPPC and CHOL are shown in **Figure 2-2** and its chemical and physical properties are also described in **ANNEX I**.

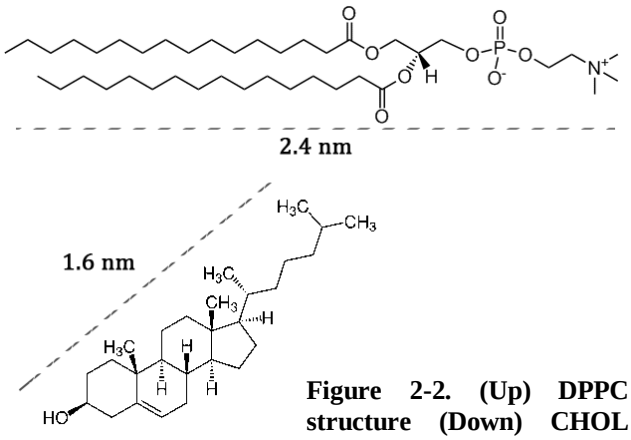

Figure 2-2. (Up) DPPC structure (Down) CHOL structure.

Performing a fast research in Web of Science's databases[13], 25 012 results for "curcumin" are shown. It is noticeable that the number of publications has increased exponentially since the 90s. The top 3 research areas are *Pharmacology pharmacy* (23.9%), *Chemistry* (20.5%) and *Biochemistry molecular biology* (15.2%). The main document types are articles (79.9%), reviews (9.6%), meeting abstracts (7.5%) and proceedings papers (2.3%). Spanish publications belong to a 1.6%. In the context of curcumin-nanoformulations, mainly vesicles[14–16] and micelles[17] are found. With regard to study the interactions of curcumin with phospholipids and other molecules, the following techniques are usually employed: ^{1}HRMN,[18–20] differential scanning calorimetry (DSC)[20,21], fluorescence quenching[20,22], molecular dynamics simulation[23], Brewster angle microscopy (BAM)[24], PM-IRRAS[24], dynamic light scattering (DLS)[17], field emission scanning electron microscopy (FESEM)[17], Raman spectroscopy[21,25–27] and UV-visible spectroscopy[27–29], among others[30–32].

Langmuir and Langmuir-Blodgett (LB) techniques represent excellent tools with which to study drug molecules at interfaces because surface pressure, area per molecule, chemical composition and temperature can be precisely controlled. Consequently, surface properties as well as miscibility studies can be performed by means of thermodynamic properties and other characterization methods, such as Atomic Force

Microscopy (AFM). However, only few articles[24,33,34] were found directly related with these techniques, and they were focused on the study of few molar fractions of CCM-DPPC binary systems, without including CHOL, or they employed other phospholipids.

In conclusion, this Master's Thesis stands for an innovative approach to study how CCM interacts with model cell membranes, enlarging the knowledge about this topic so encapsulated cell therapy and clinical trials could be better developed in the future.

3 Experimental section

3.1 Materials

The appropriate amounts of curcumin (CCM, ≥99%, Sigma-Aldrich, CAS 458-37-7), cholesterol (CHOL, ≥99%, Sigma-Aldrich, CAS 57-88-5) and dipalmitoylphosphatidylcholine (DPPC ≥99%, Sigma-Aldrich, CAS 63-89-8) were dissolved in chloroform to prepare stock solutions of 0.01 $\mu mol \cdot mL^{-1}$, 0.1 $\mu mol \cdot mL^{-1}$ and 0.1 $\mu mol \cdot mL^{-1}$, respectively. Chloroform was purchased from Macron Fine Chemicals (≥99.8%, CAS 67-66-3). Then, the binary (CCM-DPPC, CCM-CHOL and DPPC-CHOL) and ternary systems (CCM-DPPC-CHOL) were prepared by mixing proper volumes of stock solutions depending on the final molar fractions of the components in the mixture. Every time the stock solution of curcumin was used, it was sonicated 1 min in order to avoid formation of three dimensional aggregates. The molar fractions used to prepare the mixtures are listed in **Table 2-1** of **ANNEX II**.

3.2 Methods

3.2.1 Langmuir technique

The Langmuir technique, designed by Irving Langmuir in the early 20th century[35], was used to study the mimic cell membranes.

The experimental basis is simple: a trough made of a hydrophobic material is first filled with a sub-phase. After that, a certain volume of the solution that contains the compounds under studying is spread; these compounds must be insoluble in the sub-phase but soluble in a volatile solvent. Consequently, the typical compounds used are amphiphilic molecules. In addition, the spreading coefficient of the solvent on the

sub-phase must be S > 0 for a spontaneous spreading. After waiting a reasonable period of time till the spreading solvent has completely evaporated, the molecules are compressed using one or two moveable barriers. During the compression process the surface pressure is registered by means of the Whilhelmy balance. The surface pressure is defined as

$$\pi = \gamma_0 - \gamma \quad \textbf{(1)}$$

where γ_0 is the surface tension of the bare subphase and γ is the surface tension of the subphase covered by amphiphiles. Upon the compression process, the area per molecule decreases, whilst the surface pressure increases, thus obtaining the surface pressure-area per molecule (π-A) isotherm. The Langmuir isotherm provides information about the phases and phase transitions in the monolayer (**Figure 3-1**): G (gas phase, when the molecules are sufficiently far apart for lateral cohesion forces to be negligible), G-LE (coexistence of gas-liquid expanded phase), LE (liquid expanded phase, where there is some degree of cooperative interactions between the molecules), LE-LC (coexistence of liquid expanded and liquid-condensed phases), LC (liquid condensed phase, where molecules begin to be close packed), S (solid phase) and collapse.

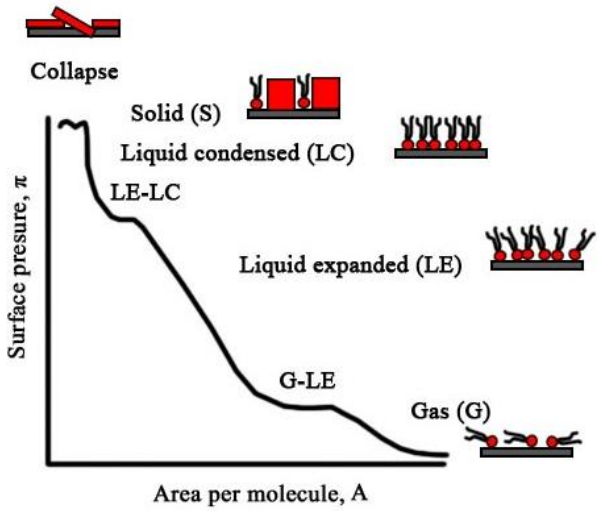

Figure 3-1. Generic surface pressure-area per molecule (π-A) isotherm. (Adapted figure from the book *Physical Chemistry of Surfaces* by Adamson and Gast[37]).

It is important to note that some of these phases and transition phases can be missed in a certain isotherm depending on many factors; the specific material that forms the monolayer, temperature, compression speed, pH, presence of salts, etc.[36,37]

In this Master's Thesis, the surface pressure-area per molecule (π-A) isotherms were recorded on a pure water sub-phase (Millipore Milli-Q purification system, resistivity 18.2 MΩ·cm) using a Teflon trough (**Figure 3-2**) contained in a constant temperature (20 ± 1 ºC) semi-clean room. An exhaustive cleaning protocol was followed before each experiment.

Figure 3-2. Image of the KSV Nima KN 2003 (580 x 145 mm^2) used in this project.

A constant initial area per molecule (130 Å·molecule^{-1}) was used for all the experiments: the appropriate volume of the solutions was spread on the water sub-phase by using Hamilton micro-syringes. In particular, the spreading coefficient of chloroform in water is 13.1 mN·m^{-1}at 20ºC. The solvent was allowed to evaporate over 15 minutes before starting the compression of the film with the trough barriers moving at a rate of 10 mm·min^{-1}. All isotherms were repeated at least three times to confirm reproducibility.

3.2.2 Mixed monolayers

A detailed study of the surface pressure-area per molecule (π-A) isotherms provides information about the miscibility of multicomponent systems. i.e. if the components are miscible, immiscible or partially miscible.

A criterion to evaluate the miscibility is the thermodynamic excess area of mixing, A^E, defined as:

$$A^E = A_{mix} - A_{ideal} \quad \textbf{(3)}$$

$$A_{ideal} = \sum_i x_i A_i \quad \textbf{(4)}$$

$$A^E = A_{mix} - \sum_i x_i A_i \quad \textbf{(5)}$$

where A_{mix} is the molecular area of the experimental mix monolayer at the chosen surface pressure, π; A_i is the molecular area of the pure components at the surface pressure π and x_i is the molar fraction. Consequently, when $A^E = 0$ the components of the monolayer are ideally miscible or totally immiscible, meanwhile if $A^E \neq 0$ the components are partially miscible. Negative deviations generally indicate attractive interactions between the components, while positive deviations generally indicate repulsive interactions. Therefore, this criterion only provides information about having

i) ideal miscible or totally immiscible components in the monolayer or ii) partially miscible monolayers. In the case of having $A^E = 0$, it is necessary to use another criterion in order to determine whether the components are miscible or immiscible. The collapse surface pressure, π_{col}, of the mixed monolayers can be employed to elucidate between miscibility and immiscibility. Consequently, if the components are ideally miscible, the collapse will occur at intermediate pressures between the π_{col} of the pure components, being proportional to the molar fraction of the components in the mixture (**Figure 3-3, a**), whereas if the components are totally immiscible, the collapse will occur at the π_{col} of the component with the lowest π_{col} (**Figure 3-3, b**).

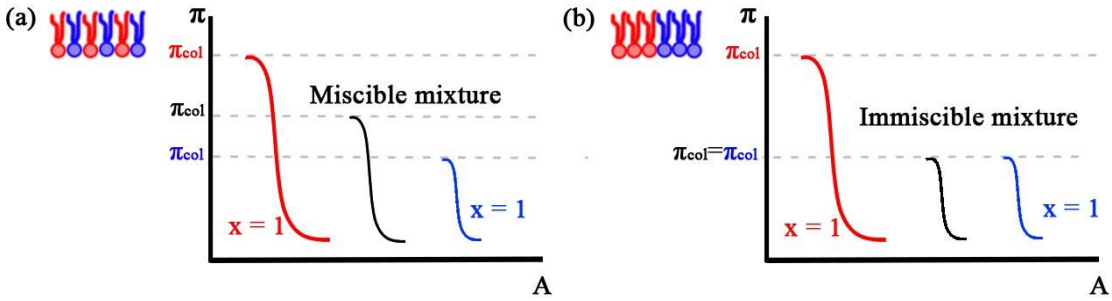

Figure 3-3. Theoretical π-A isotherms for binary monolayers of (a) ideal miscible mixture and (b) totally immiscible mixture.

The influence of the miscibility / immiscibility of the components in the collapse surface pressure of the mixed monolayer can be explained in terms the surface phase rule, proposed by Defay and Crisp[38] and derived from the ordinary phase rule in the bulk solution. At constant temperature and pressure, and in absence of electrical and external potentials, the number of degrees of freedom, *f*, will be

$$f = C^B + C^S - P^B - P^S + 1 \qquad (2)$$

where C^B is the number of components in the system, C^S is the number of components restricted to the surface, P^B is the number of phases in the system, P^S is the number of phases in the surface and *1* the only variable (surface tension). It should be noted that this criterion determines miscibility at a transition between two states, preferentially at collapse pressure, but also, by extension, at LE-LC transition because the collapse is not always easily measurable.

For example, the phase rule can be applied at the collapse for a binary system of components A and B, assuming that the monolayer and the collapsed phase are in equilibrium. When the components are completely miscible, the system possesses one degree of freedom and a first order relation between the considered transition pressure

and the composition is observed; thus, there is no deviation from ideal behaviour and the bidimensional analogue of Raoult's law is obeyed. When the components are completely immiscible, both components are squeezed out and the collapsed phases consist of the two pure components. Consequently, there are no degrees of freedom. Finally, when the components are partially miscible, in the range of immiscibility the transition pressure is also invariant of the composition.[39,40]

Some difficulties associated with the study of miscibility are the non-reproducibility of the isotherms, the formation of disordered multilayers, the formation of complexes in the reaction, the formation of new phases or the presence of rigid films where the overflowing of the sub-phase can be mistaken with the collapse.

Additionally, the mixture of the components is also associated with the energy of the mixing process. This was first analysed by Goodrich.[41] At constant p and T, the Gibbs surface excess energy of mixing, $\Delta {G_m}^E$ can be defined as

$$\Delta G_m^E = \int_0^\pi A_{mix} d\pi - \sum_i x_i \int_0^\pi A_i d\pi \quad \textbf{(6)}$$

Negative values of $\Delta {G_m}^E$ indicate strong interactions between the components, while positive values reveal weaker or even repulsive interactions between the two components in the mixed film in comparison with the pure compounds.

Taking into account that

$$\Delta G^{ideal}{}_m = RT \sum_i x_i \ln x_i \quad \textbf{(7)}$$

the Gibbs energy of mixing can be calculated as

$$\Delta G_m = \Delta G_m^E + \Delta G^{ideal}{}_m \quad \textbf{(8)}$$

Other relevant parameter that can be calculated from the isotherms is the compressibility coefficient, C_s, and, thus, the Young modulus, K_s.

$$Cs = -\frac{1}{A}\left(\frac{dA}{d\pi}\right)_T \quad \textbf{(9)}$$

$$Ks = Cs^{-1} = -A\left(\frac{d\pi}{dA}\right)_T \quad \textbf{(10)}$$

Accordingly to the classification of David and Rideal[36], the values of K_s ranging 10-50 mN·m^{-1} correspond to the LE phase, the values of K_s ranging 100-250 mN·m^{-1} correspond to the LC phase and values up to 1000 mN·m^{-1} correspond to the S phase.

3.2.3 Langmuir-Blodgett technique

A Langmuir monolayer at the air-water interphase can be transferred onto a solid substrate (LB film). Here, the substrate is immersed in or withdrawn from the water sub-phase, and the final thickness of the LB film can be controlled through the number of dipping processes carried out.

In this Master's Thesis, the Langmuir films were transferred onto mica substrates to be subsequently characterized by AFM. Mica was chosen because it is a very flat and therefore it is a very appropriate substrate for the films topography characterization. Sheets were provided by Electron Microscopy Sciences Company (Cat. #71851-05, sheet size 1" x 3"; 25 x 75 mm and thickness 0.26-0.31 mm). Consequently, each mica substrate was cut by using scissors into ca. 1 x 1 cm^2 pieces and was cleaved with a cello tape prior to its use. The monolayers at the air-water interface were transferred at a constant surface pressure by the vertical dipping method (emersion, as can be seen in **Figure 3-4**). Dipping speed was 2 $mm \cdot min^{-1}$.

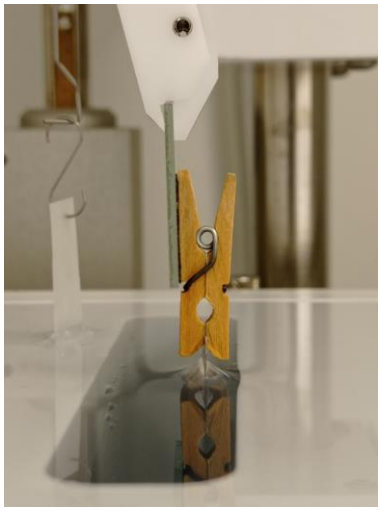

Figure 3-4. Dipping experimental setup; mica substrate is held by wood tweezers and first immersed in the water sub-phase. The Wilhelmy paper plate can be seen in the background.

3.2.4 Atomic Force Microscopy

Atomic Force Microscopy (AFM) was invented in 1986 by G. Binnin, C.F. Quate and C. Gerber in order to overcome the limitations of Scanning Tunneling Microscopy (STM): to avoid high vacuum systems and to scan poor conductive materials such as biomolecules. The basic concept of AFM is the measurement of forces (attractive or repulsive) between a sharp tip attached to a cantilever and a sample surface. A laser is reflected at the rear side of the cantilever and the deflection originated by these forces is monitored by a position-sensitive photodiode.[42]

AFM technique was used to obtain topographic images of the LB films that could provide additional information about the miscibility of the three components, in particular after the transference process. The experiments were performed by means of a Multimode 8 microscope equipped with a Nanoscope V control unit from Bruker at a

scan rate of 1.0–1.2 Hz, using Tapping mode. This microscope belongs to the Advanced Microscopy Laboratory (LMA) at the University of Zaragoza. The data were collected using RTESPA-150 tips (nominal frequency of 150 kHz, from Bruker) for the images recorded in air. Images were typically recorded with scan rates of 1 $Hz \cdot line^{-1}$, 512x512 lines and force ranging 0.2-2 nN.

The images were processed with Gwyddion 64Bit Software. Differences in height between monolayer domains were determined by performing section analysis.

4 Results and discussion

4.1 Single monolayers

Each of the compounds here studied (CCM, DPPC and CHOL) forms Langmuir monolayers at the air-water interface, i.e. the layer-forming molecules are practically insoluble in the water sub-phase and these molecules are capable of forming a two-dimensional film at the interface upon the compression process. **Figure 4-1** shows the surface pressure-area per molecule (π-A) isotherms and the Ks-π plots for each of the single monolayers here studied.

For the CCM single monolayer, the lift-off in the isotherm occurs at ca. 0.23 $nm^2 \cdot molecule^{-1}$; this area denotes the first value for the area per molecule at which the surface pressure can be detected upon the compression process, i.e. $\pi \cong 0.5\ mN \cdot m^{-1}$, and it corresponds to the transition from a G to LE phase. A change of slope at ca. 15 $mN \cdot m^{-1}$ is indicative of a phase transition between LE-LC phases. This can be better noticed in the Ks-π plots: below 15 $mN \cdot m^{-1}$, Ks is about 20 $mN \cdot m^{-1}$ (LE phase), while above 15 $mN \cdot m^{-1}$, Ks reaches a maximum of 83 $mN \cdot m^{-1}$. Finally, the collapse occurs at a surface pressure of 51 $mN \cdot m^{-1}$.

With regard to the CHOL single monolayer, the lift-off in the isotherm occurs at ca. 0.36 $nm^2 \cdot molecule^{-1}$. Beyond this point, the surface pressure increases monotonously until the collapse is reached at 46 $mN \cdot m^{-1}$. In the Ks-π plot, the transition between LE-LC phases can be noticed at very low surface pressure, ca. 2 $mN \cdot m^{-1}$, and the transition between LC-S phases occurs at ca. 8 $mN \cdot m^{-1}$. The maximum Ks reached for CHOL is 469 $mN \cdot m^{-1}$.

For the DPPC single monolayer, the lift-off in the isotherm occurs at ca. 1.09 $nm^2 \cdot molecule^{-1}$. The change of slope at 5-10 $mN \cdot m^{-1}$ is indicative of a phase transition between LE-LC phases. Finally, the collapse occurs at 67 $mN \cdot m^{-1}$. In the Ks-π plots, LC phase is reached at ca. 15 $mN \cdot m^{-1}$. The maximum Ks is 247 $mN \cdot m^{-1}$, near the limit between LC-S phases.

In conclusion, CCM presents the lower values of Ks, i.e. the most expanded phase, DPPC presents intermediate values of Ks, i.e. the monolayer remains in a LC phase without reaching S phase, and CHOL presents the higher values of Ks, i.e. the most condensed phase.

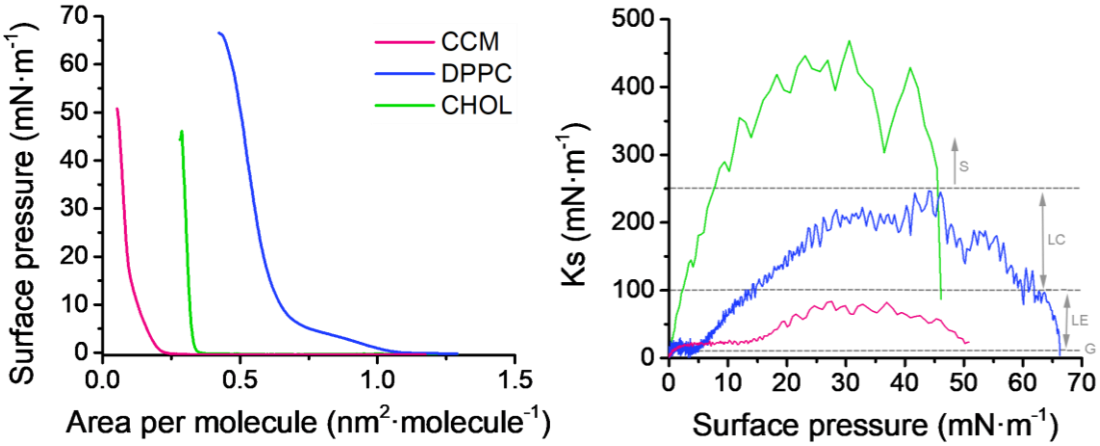

Figure 4-1. (Left) π-A isotherms for the monolayers of CCM, DPPC and CHOL at 20ºC. (Right) Ks-π plot for the monolayers of CCM, DPPC and CHOL.

4.2 Binary monolayers

Figure 4-2 shows the surface pressure-area per molecule (π-A) isotherms and the Ks-π plots for each of the binary monolayers here studied. In **ANNEX III**, the collapse surface pressure-molar fraction plots for all the binary systems are represented, including a comparison between the experimental values and the ideal ones.

For the CCM-DPPC binary system, the addition of CCM to DPPC results in more condensed isotherms (lower areas per molecule at a certain surface pressure). The characteristic plateau in the DPPC monolayer turns in a slope change in the mixed films. With regard to the collapse surface pressure, deviations from ideality are obtained, indicative of a partial miscibility between CCM and DPPC. Also, the transition between the LE and the LC phases occurs at higher pressures for the CCM-DPPC mixtures than for the pure DPPC monolayer. The reason of these observations is

the clear tendency of the CCM to decrease the Ks values for the CCM-DPPC mixtures at a given surface pressure, i.e. the monolayers are less compressible under the presence of CCM. The phases and phase transitions can be better detected in the Ks-π plots: Ks values tend to decrease at a certain surface pressure as CCM is added.

For the CCM-CHOL binary system, the tendency is similar to the previous case: the addition of CCM to CHOL results in more condensed isotherms that resembles the isotherm obtained for a single monolayer of CCM. With regard to the collapse surface pressure, deviations from ideality are obtained which is indicative of partially miscible components in the mixed monolayers. Taking into account the Ks-π plots: as x_{CCM} increases, Ks values decrease, i.e. the monolayers are in a more expanded state.

According to the DPPC-CHOL binary system, the addition of CHOL to DPPC results in more condensed isotherms that resembles the isotherm obtained for a single monolayer of CHOL. With regard to the collapse surface pressure, deviations from ideality occur, which is indicative of partially miscible components in the mixed monolayers. In contrast with the previous binary systems, here the DPPC-CHOL monolayers exhibit a non-linear dependence of Ks values with the molar fraction. This is in good agreement with previous observations in which CHOL is known to play a crucial role in the fluidity of the phospholipid membrane increasing the structural order of the alkyl chains of the phospholipid[43,44], having the opposite effect on phospholipids in the gel phase.[45–47]

In conclusion, CCM yields monolayers with a lower Ks (or higher Cs) when added to DPPC and CHOL. On the other hand, intermediate molar fractions of CHOL causes a condensing effect when added at to DPPC. Moreover, the change of the collapse surface pressure with the molar fraction in all the cases (CCM-DPPC, CCM-CHOL, DPPC-CHOL) indicates that the two components are, at least, partially miscible according to the Crisp's rule.

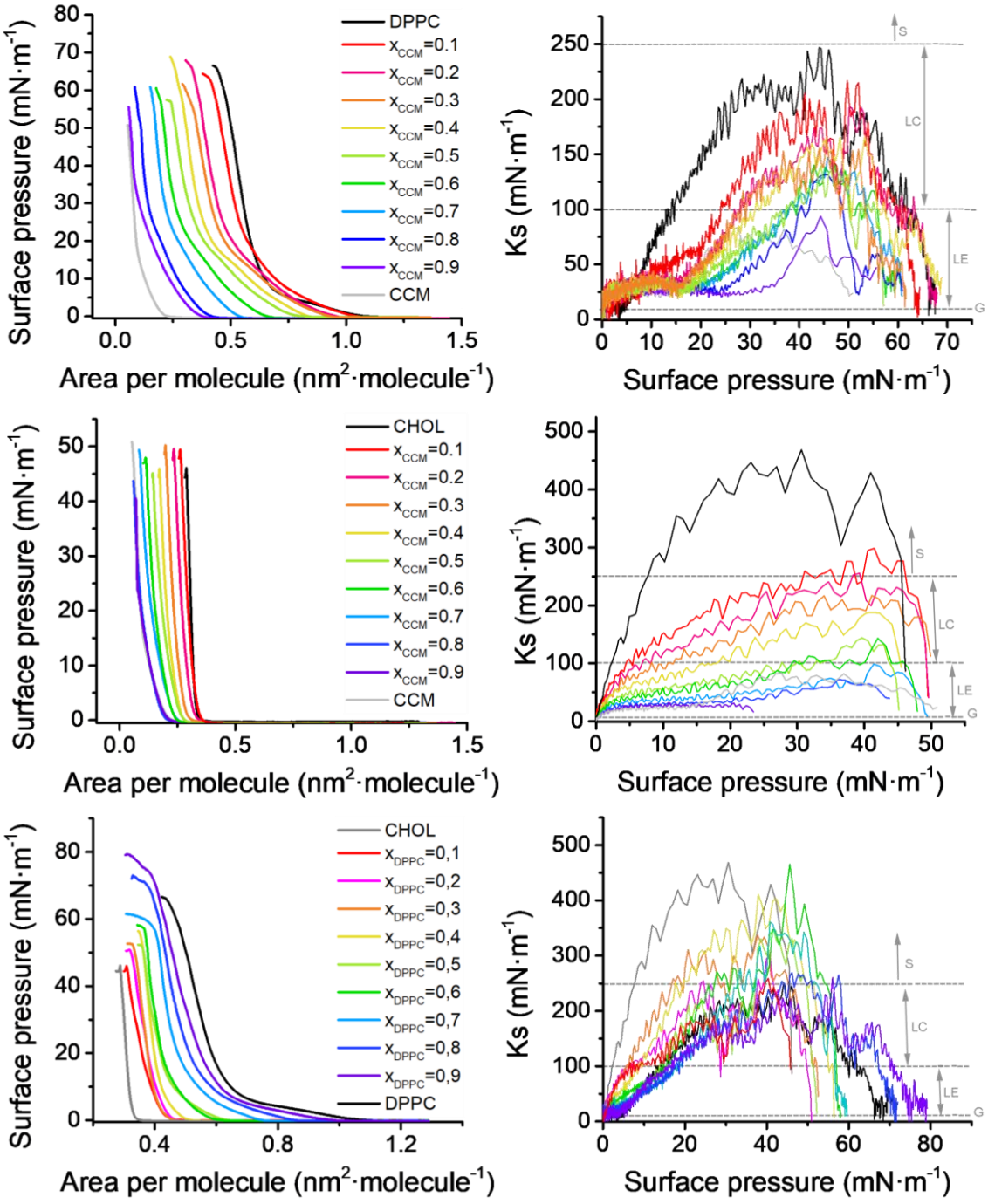

Figure 4-2. (Left) π-A isotherms for the CCM-DPPC, CCM-CHOL and DPPC-CHOL binary systems at 20ºC. (Right) Ks-π plots the CCM-DPPC, CCM-CHOL and DPPC-CHOL binary systems.

As it is seen in section **3.2.2 Mixed monolayers**, further information about the mixing behaviour of multicomponent systems can be extracted from the thermodynamic parameters: A^E, $\Delta {G_m}^E$ and ΔG_m.

For all the binary systems, the values of A^E were calculated using **Equation 3, Equation 4** and **Equation 5** for the surface pressures of 5, 10, 15, 20, 30 and 40 mN·m^{-1}. According to the CCM-DPPC binary system (**Figure 4-3, a**), as the surface

pressure increases, A^E decreases. For surface pressures below 30 mN·m^{-1}, A^E presents positive values, indicating repulsive interactions between CCM and DPPC, while above 30 mN·m^{-1}, A^E shows negative values, revealing attractive interactions and the formation of a more compact monolayer than the ideal one. In both cases, the deviations from ideality prove a non-ideal behaviour and a partial miscibility between the two components in the film. Additionally, the presence of two minima at x_{CCM} = 0.2 and 0.8 suggests phase segregation, i.e. there is a particularly favoured organization of the components at these compositions. With regard to the CCM-CHOL binary system (**Figure 4-3, b**), the values are much lower than the ones of the previous system. At molar fractions above x_{CCM} = 0.2, negative A^E are obtained at all the surface pressures, and the values become more negative as the surface pressure increases, achieving a minimum at x_{CCM} = 0.8. Finally, for the DPPC-CHOL binary system (**Figure 4-3, c**), above x_{DPPC} = 0.3 A^E shows negative values, thus indicating attractive interactions and partially miscibility between the components. In addition, the presence of two minima at x_{DPPC} = 0.4 and 0.6 is indicative of some degree of phase segregation.

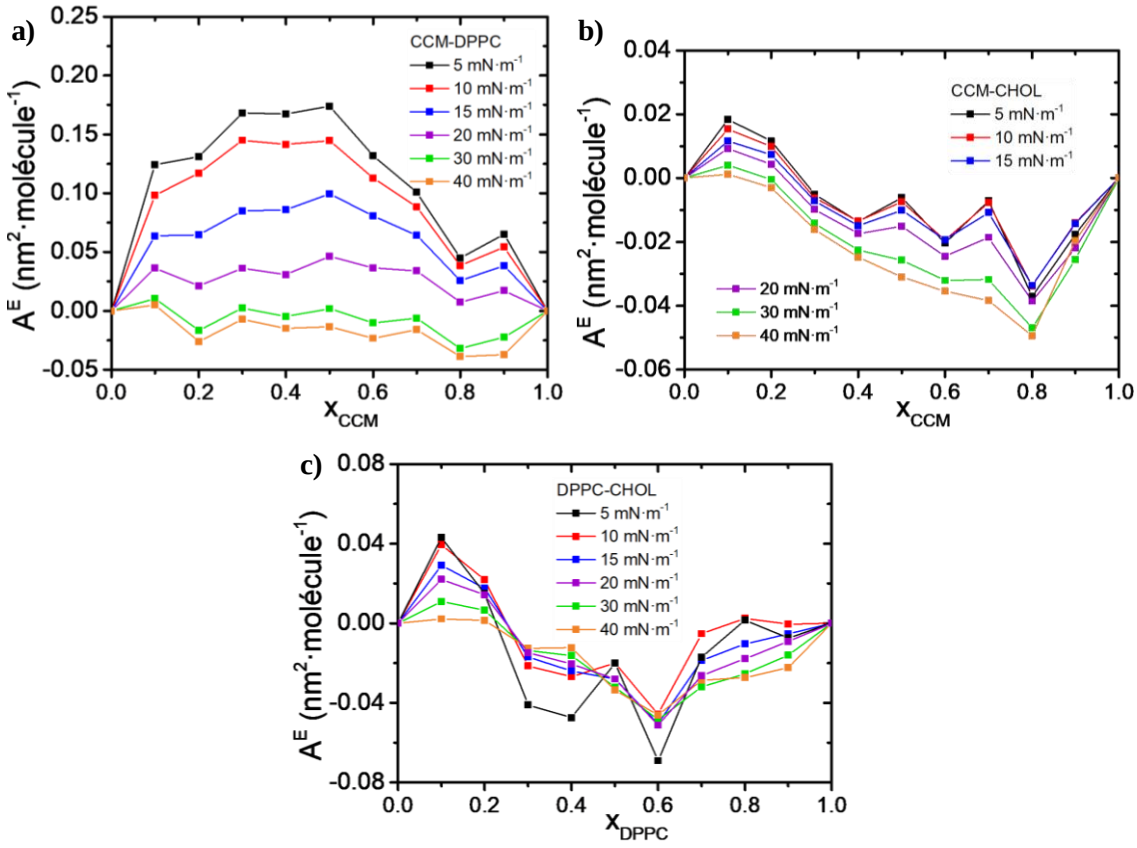

Figure 4-3. Excess molecular area vs. composition of the (a) CCM-DPPC, (b) CCM-CHOL and (c) DPPC-CHOL binary systems.

The values of excess Gibbs energy of mixing were calculated using **Equation 6** for the surface pressures of 5, 10, 15, 20, 30 and 40 mN·m^{-1}. According to the CCM-DPPC binary system (**Figure 4-4, a**), as the surface pressure increases, $\Delta G_m{}^E$ increases and it is positive for the whole range of molar fractions, suggesting that the interactions between components in the binary systems are more repulsive than in the single monolayers. On the contrary, for the CCM-CHOL (**Figure 4-4, b**) and DPPC-CHOL (**Figure 4-4, c**) binary systems, in all molar fraction ratios $\Delta G_m{}^E$ decreases both as the surface pressure increase and the molar ratio of CCM increases, which proves that the films components mix favourably and that the interactions in multicomponent monolayers are more attractive as compare to those in the films without CHOL. In the CCM-CHOL binary system the most negative values of $\Delta G_m{}^E$ are present at x_{DPPC} = 0.8, while in the DPPC-CHOL binary system the most negative values of $\Delta G_m{}^E$ are present at x_{DPPC} = 0.6, thus these monolayers exhibit the highest thermodynamic stability. These results are in good agreement with the conclusions obtained from A^E values.

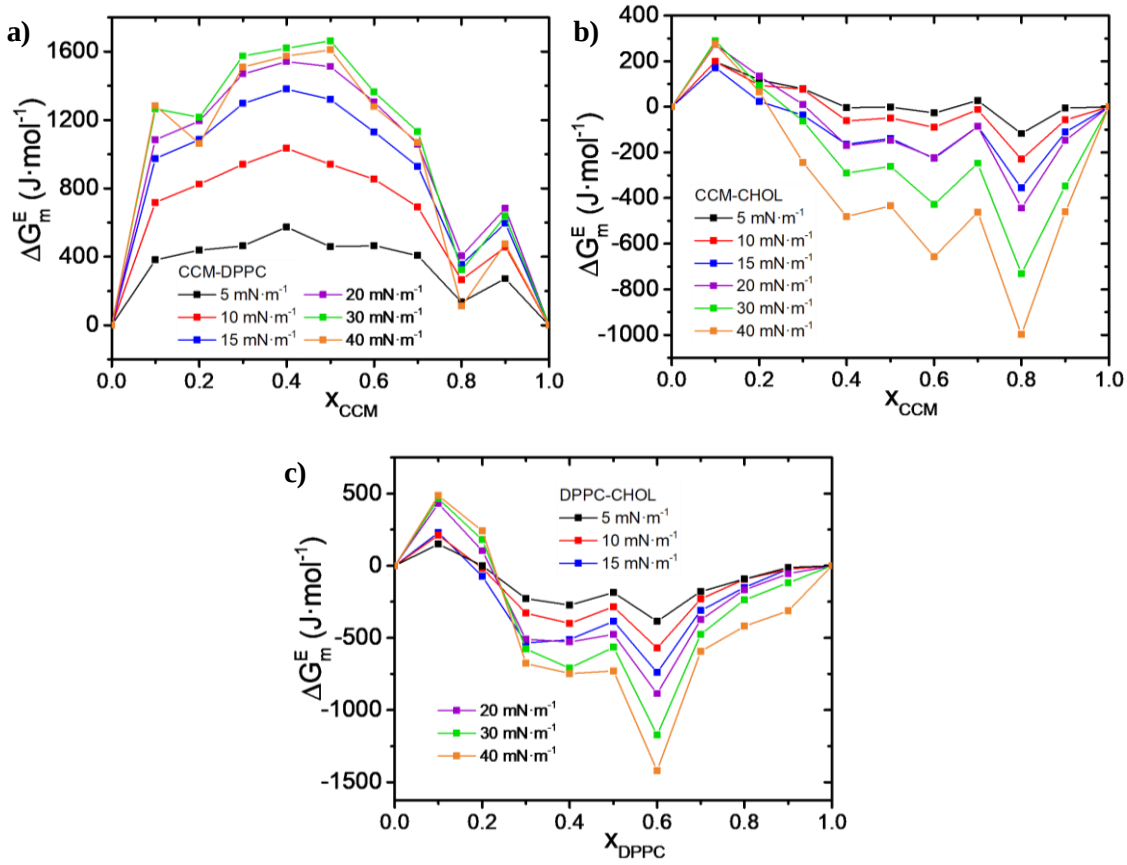

Figure 4-4. Excess Gibbs energy of mixing vs. composition of the (a) CCM-DPPC, (b) CCM-CHOL and (c) DPPC-CHOL binary systems.

Finally, for all the binary systems the values of ΔG_m were calculated using **Equation 7** and **Equation 8** and they were plotted as previously. Accordingly with the $\Delta {G_m}^E$ results, in the CCM-DPPC binary system (**Figure 4-5, a**), as surface pressure increases, ΔG_m increases except for the molar fraction of $x_{CCM} = 0.8$. It is important to note that, as the molar fraction increases, ΔG_m decreases, indicating attractive interactions between molecules. With respect to CCM-CHOL (**Figure 4-5, b**) and DPPC-CHOL (**Figure 4-5, c**) binary systems, for the whole range of molar fractions ΔG_m is negative and, as surface pressure increases, ΔG_m decreases.

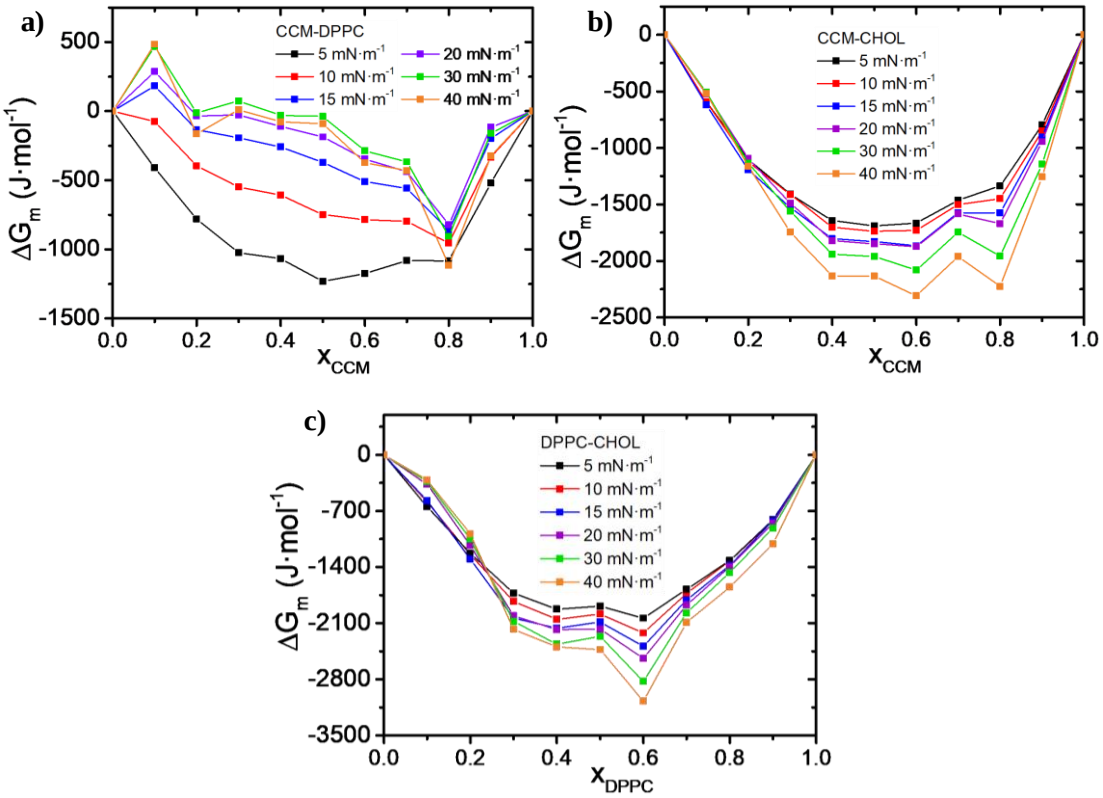

Figure 4-5 Gibbs energy of mixing vs. composition of the (a) CCM-DPPC, (b) CCM-CHOL and (c) DPPC-CHOL binary systems.

In the interpretation of the obtained experimental results, two effects may occur simultaneously: 1) the steric effect, i.e. the orientation of the molecules, and 2) the energetic effect, i.e. the interaction between the molecules. According to the CCM-DPPC binary system, for the A^E the steric effect prevails over the energetic effect because, as the surface pressure increases, the A^E decreases. On the other hand, for the $\Delta {G_m}^E$ and ΔG_m the energetic effect prevails over the steric effect because, as the surface pressure increases, the energy increases. This suggests that the addition of CCM to DPPC destabilizes the monolayer until the CCM collapses and it is expelled out of the monolayer (this explains why A^E is negative at 40 mN·m^{-1}). Even though the CCM-

DPPC binary system seems to be less stable than CCM-CHOL and DPPC-CHOL binary systems, this can be an advantage when referring to cell membranes: once CCM penetrates into the membrane, it will generate repulsion between the lipids, making the membrane more permeable.

4.3 Ternary monolayers

To the best of our knowledge, ternary systems of CCM-DPPC-CHOL have not been studied before. Therefore, in this Master's Thesis a deep study has been performed. To get a representative ternary diagram, well distributed 40 points were selected (see **ANNEX** II).

In **ANNEX IV** all the surface pressure-area per molecule (π-A) isotherms at the different molar fractions of CCM are presented. Furthermore, the influence of CHOL and DPPC at the same CCM molar fraction is also studied; as in the case of the binary mixtures, the addition of both CCM and CHOL causes more condensed isotherms. Moreover, the collapse surface pressure changes at different molar fraction compositions, so according to the Crisp's rule CCM, DPPC and CHOL are components at least partially miscible in the ternary mixtures.

The thermodynamic analysis (A^E, ${\Delta G_m}^E$, ΔG_m and *Ks*) of the ternary systems was combined with the one obtained for the binary systems. The equations described in section **3.2.2 Mixed monolayers** were applied.

A^E versus film composition for the whole range of surface pressures (5, 10, 15, 20, 30, 40 $mN \cdot m^{-1}$) is shown in **Figure 4-6**. At low pressures (5-15 $mN \cdot m^{-1}$), negative deviations from the ideal behaviour can be observed at low molar fractions of CCM ($x_{CCM}<0.3$, $0.3<x_{CHOL}<0.8$, $0.2<x_{DPPC}<0.7$, purple regions), but also at high molar fractions of CCM ($x_{CCM}>0.6$, $0.1<x_{CHOL}<0.3$, $x_{DPPC}<0.2$, purple regions) indicating partial miscibility and attractive interactions between the components in the monolayer. On the other hand, positive deviations are present at low molar fractions of CHOL ($x_{CHOL}<0.2$, green, yellow and red regions), providing repulsive interactions between the components in the monolayer. At intermediate pressures (15-20 $mN \cdot m^{-1}$), negative deviations are spread to the center of the ternary diagram and the region of low molar fraction of CHOL becomes less positive. At high pressures (20-40 $mN \cdot m^{-1}$), negative deviations (purple regions) are present in almost all the ternary diagram, while less

negative deviations (blue regions) are present in the vertices and at high molar fractions of CCM and low molar fractions of CHOL (x_{CCM}>0.5, x_{CHOL}<0.5 and 0.3<x_{CHOL}<0.6). Summarizing, as the surface pressure increases, A^E decreases so the attractive interactions between the components increase.

In terms of the steric effect, the less stable ternary monolayers are x_{CCM}-x_{DPPC}-x_{CHOL} = 0.9-0.05-0.05 (A^E = 0.43 nm^2·molecule^{-1} at 5 mN·m^{-1}) and x_{CCM}-x_{DPPC}-x_{CHOL} = 0.2-0.7-0.1 (A^E = -0.20 nm^2·molecule^{-1} at 5 mN·m^{-1}), while the most stable ternary monolayers are x_{CCM}-x_{DPPC}-x_{CHOL} = 0.7-0.1-0.2 and x_{CCM}-x_{DPPC}-x_{CHOL} = 0.4-0.4-0.2 (A^E = -0.04 nm^2·molecule^{-1} at 40 mN·m^{-1}).

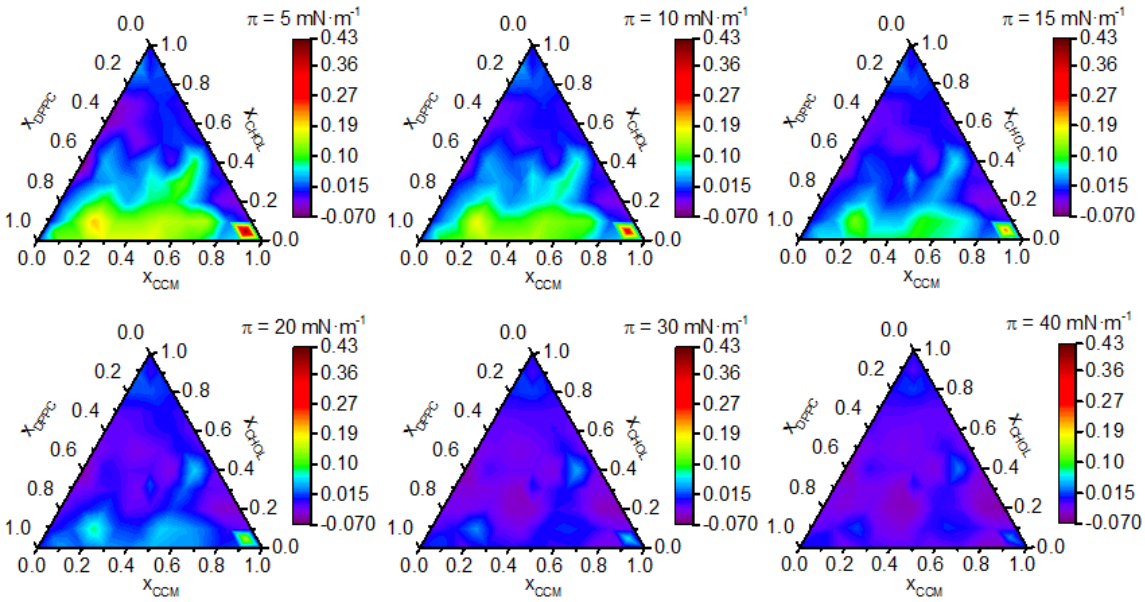

Figure 4-6. Excess molecular area vs molar fraction in ternary and binary systems at different surface pressures, 20ºC.

In **Figure 4-7**, $\Delta G_m{}^E$ versus film composition for the whole range of surface pressures (5, 10, 15, 20, 30, 40 mN·m^{-1}) is plotted. The mapping is similar for all the cases: negative deviations of $\Delta G_m{}^E$ are present at low molar fractions of CCM (x_{CCM}<0.3, 0.3<x_{CHOL}<0.7, 0.3<x_{DPPC}<0.7, purple regions), but also at high molar fractions of CCM (x_{CCM}>0.7, 0.1<x_{CHOL}<0.3, x_{DPPC}<0.2, purple regions), which is in good agreement with the conclusions obtained from the A^E values. On the other hand, positive deviations are present at low molar fractions of CHOL (x_{CHOL}<0.2, green, yellow and red regions). In general, as the surface pressure increases, $\Delta G_m{}^E$ reaches both more positive values (from $\Delta G_m{}^E$ = 1610 J·mol^{-1} at 5 mN·m^{-1} to $\Delta G_m{}^E$=5097 J·mol^{-1} at 40 mN·m^{-1}) and more negative values (from $\Delta G_m{}^E$= -390 J·mol^{-1} at 5 mN·m^{-1} to $\Delta G_m{}^E$= -1420 J·mol^{-1} at 40 mN·m^{-1}).

In terms of energetic effect, the less stable ternary monolayers are x_{CCM}-x_{DPPC}-x_{CHOL} = 0.9-0.05-0.05 ($\Delta G_m{}^E$ = 5090 J·mol^{-1} at 40 mN·m^{-1}) and x_{CCM}-x_{DPPC}-x_{CHOL} = 0.2-0.7-0.1 ($\Delta G_m{}^E$ = 2402 J·mol^{-1} at 40 mN·m^{-1}), while the most stable ternary monolayers are x_{CCM}-x_{DPPC}-x_{CHOL} = 0.4-0.2-0.4 ($\Delta G_m{}^E$ = -824 J·mol^{-1} at 40 mN·m^{-1}) and x_{CCM}-x_{DPPC}-x_{CHOL} = 0.2-0.3-0.5 ($\Delta G_m{}^E$ = -765 J·mol^{-1} at 40 mN·m^{-1}).

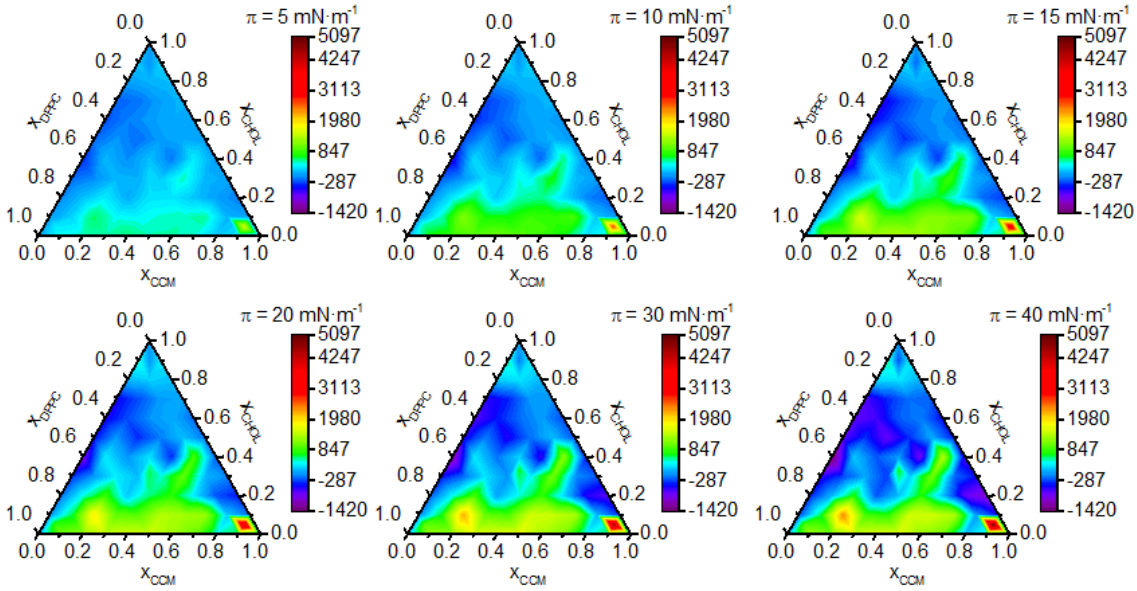

Figure 4-7. Excess Gibbs energy of mixing vs molar fraction in ternary and binary systems at different surface pressures.

In **Figure 4-8**, ΔG_m versus film composition is plotted. The most negative values of ΔG_m are present in the center of the triangle (purple regions), while the most positive values are present in the vertices of the triangle (yellow and red regions). This can be explained as follows: the vertices correspond to the single monolayers of each component, so the interaction between the molecules of the same component is higher than the interaction between different components, which are in very low molar fraction in these regions. Particularly, the vertex of CCM shows the most positive values, thus it is the region with less stability. As already observed for the $\Delta G_m{}^E$ values, as the surface pressure increases, ΔG_m reaches both more positive values (from ΔG_m= 623 J·mol^{-1} at 5 mN·m^{-1} to ΔG_m = 4093 J·mol^{-1} at 40 mN·m^{-1}) and more negative values (from ΔG_m= -2710 J·mol^{-1} at 5 mN·m^{-1} to ΔG_m= -3420 J·mol^{-1} at 40 mN·m^{-1}).

Therefore, the less stable ternary monolayers are x_{CCM}-x_{DPPC}-x_{CHOL} = 0.9-0.05-0.05 (ΔG_m= 4123 J·mol^{-1} at 40 mN·m^{-1}) and x_{CCM}-x_{DPPC}-x_{CHOL} = 0.2-0.7-0.1 (ΔG_m = 435 J·mol^{-1} at 40 mN·m^{-1}), while the most stable ternary monolayers are

x_{CCM}-x_{DPPC}-x_{CHOL} = 0.4-0.2-0.4 (ΔG_m = -3412 J·mol^{-1} at 40 mN·m^{-1}) and x_{CCM}-x_{DPPC}-x_{CHOL} = 0.2-0.3-0.5 (ΔG_m= -3292 J·mol^{-1} at 40 mN·m^{-1}).

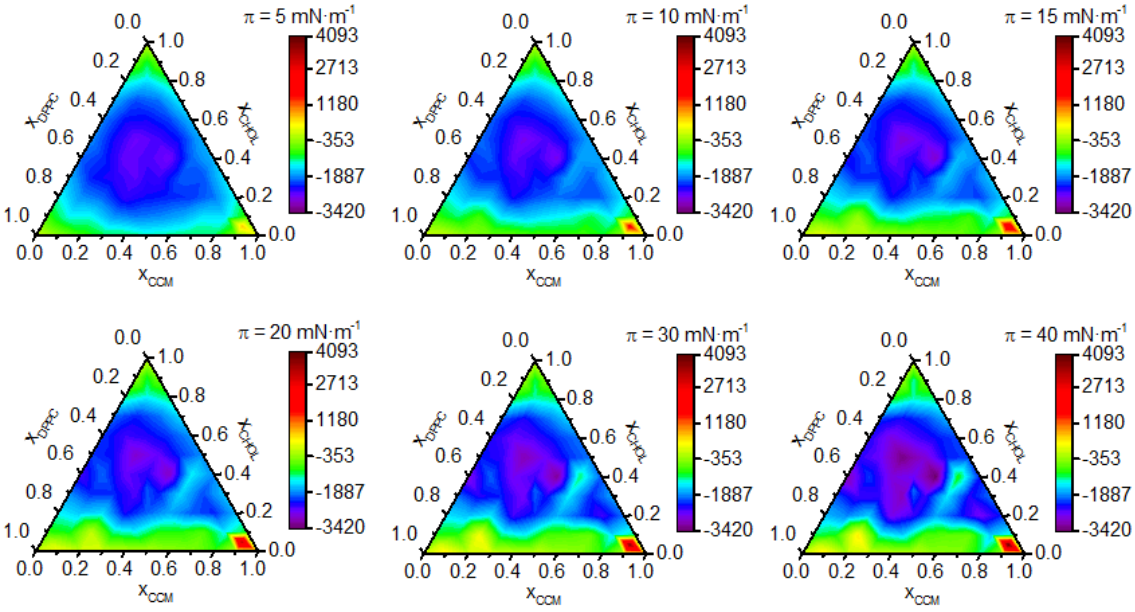

Figure 4-8. Gibbs energy of mixing vs molar fraction in ternary and binary systems at different surface pressures.

To conclude this thermodynamic analysis, **Figure 4-9** represents *Ks* versus film composition for the whole range of surface pressures (5, 10, 15, 20, 30, 40 mN·m^{-1}). At low pressures (5-15 mN·m^{-1}), LE phase is present at x_{CHOL}<0.5 and x_{DPPC}>0.5 (purple regions); as the molar fraction of CHOL increases, LE-LC transition phase (dark blue regions) and LC phase (light blue regions) appear. At intermediate pressures (15-20 mN·m^{-1}), the values became more positive at low molar fraction of CCM (green and yellow regions), so the phases are more compressed. At high pressures (20-40 mN·m^{-1}), the LE phase is displaced to the vertex of CCM; as the molar fraction of CCM decreases, the phases are more compressed until they reach the LC-S transition phase (orange and red regions). In general, as the surface pressure increases, the monolayers are more compressed.

In this case, the more compressed monolayers are x_{CCM}-x_{DPPC}-x_{CHOL} = 0.1-0.4-0.5 (*Ks* = 338 mN·m^{-1} at 40 mN·m^{-1}) and x_{CCM}-x_{DPPC}-x_{CHOL} = 0.1-0.5-0.4 (*Ks* = 331 mN·m^{-1} at 40 mN·m^{-1}), while the most expanded monolayers are x_{CCM}-x_{DPPC}-x_{CHOL} = 0.9-0.05-0.05 (*Ks* = 16 mN·m^{-1} at 15 mN·m^{-1}) and x_{CCM}-x_{DPPC}-x_{CHOL} = 0.9-0.05-0.05 (*Ks* = 20 mN·m^{-1} at 20 mN·m^{-1}).

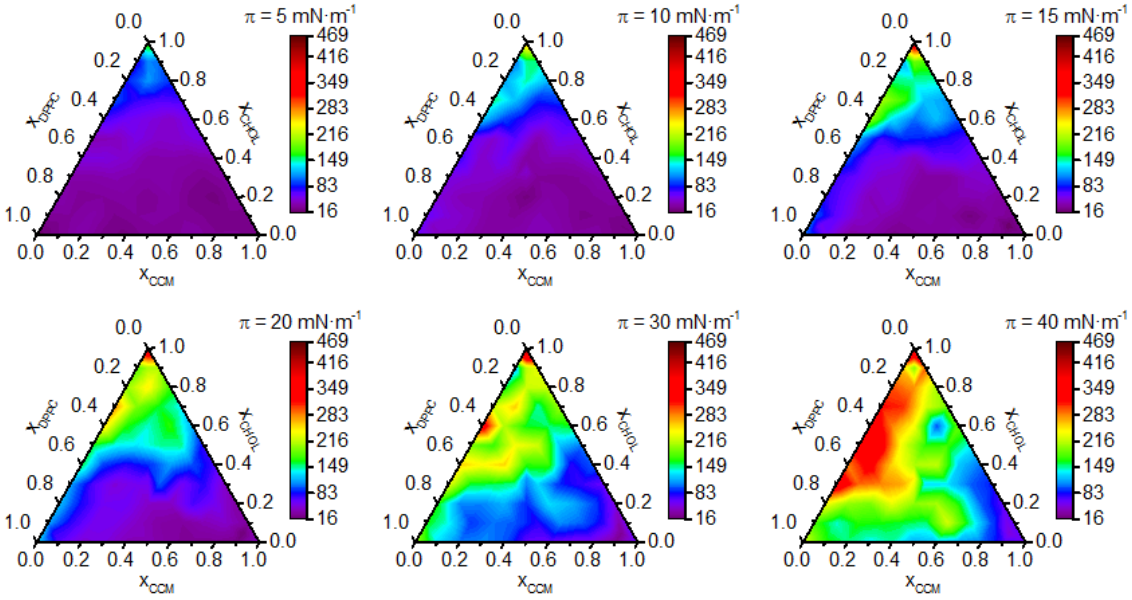

Figure 4-9. *Ks* vs molar fraction in ternary and binary systems at different surface pressures.

As already mentioned in section 2 **Introduction**, Eukaryotic plasma membranes contain up to one molecule of cholesterol for every phospholipid molecule, so it is important to analyse in detail the regions with DPPC-CHOL (1:1). In the tables of **ANNEX V** the thermodynamic parameters (A^E, $\Delta {G_m}^E$, ΔG_m and *Ks*) are presented for the mixtures maintaining constant the composition of DPPC-CHOL (1:1), i.e. x_{CCM} = 0.2, 0.33, 0.4, 0.6, 0.8 and 0.9. The most negative values are obtained at 40 mN·m^{-1}: A^E = -0.023 nm^2·molecule^{-1} (x_{CCM} = 0.8), $\Delta {G_m}^E$ = -247 J·mol^{-1} (x_{CCM} = 0.2) and ΔG_m = -2836 J·mol^{-1} (x_{CCM} = 0.2). In general, the most stable monolayers are the ones with low molar fractions of CCM at high surface pressures. The most compressed monolayer is the one with x_{CCM} = 0.2 at 30 mN·m^{-1} (*Ks* = 257 mN·m^{-1}, LC phase), while the less compressed monolayer is the one with x_{CCM} = 0.9 at 15 mN·m^{-1} (*Ks* = 16.4 mN·m^{-1}, LE phase). Taking into account that the biological surface pressure is ca. 30 mN·m^{-1},[48] the most favoured interactions between the components are present in the monolayer with x_{CCM} = 0.2 (DPPC-CHOL 1:1).

4.4 AFM

As it is said in section **3.2.3 Langmuir-Blodgett technique**, selected LB films were transferred onto mica substrates by vertical dipping. Therefore, the hydrophilic groups in the monolayer will contact with the mica surface. The transferences were performed at 30 mN·m^{-1} as it is considered a relevant biological surface pressure.[48] Although, LB films were also transferred at 20 mN·m^{-1} to study the influence of the

surface pressure in the monolayers. In order to evaluate the morphology of the LB films formed, a systematic study of their topographical features in air conditions was carried out by AFM.

Figure 4-10 shows AFM images of CCM, DPPC and CHOL single monolayers. CCM single monolayer exhibits the formation of 3D structures with ca. 30 nm in height as well as more compacted areas and the presence of holes of ca. 5 nm. These evidences reveal that at 30 $mN \cdot m^{-1}$ CCM single monolayer has collapsed. Whilst, at 20 $mN \cdot m^{-1}$ (**Figure 4-11**) the monolayer of CCM is less collapsed; 3D structures of ca. 10 nm in height and more homogenous and compact areas with a ca. 1.2 nm thickness are observed. For the DPPC single monolayer, characteristic geometrical patterns (ca. 1 nm in height) related to the LC phase are present. This is in agreement with previous literature where DPPC shows two main lamellar phases, the solid crystalline (L_β) and the liquid-crystalline (L_α). By varying the temperature, two phase transitions are distinguished that could correspond to the transitions between S-LC phases and LC-LE phase. The presence of domain boundaries in the LC phase and its disappearance in the LE phase suggests that they form part of the structure of the monolayer and that they are related to the LC-LE phase transition process.[49] Finally, CHOL single monolayer exhibits a very homogenous film (Rq-RMS roughness = 0.07 ± 0.02 nm).

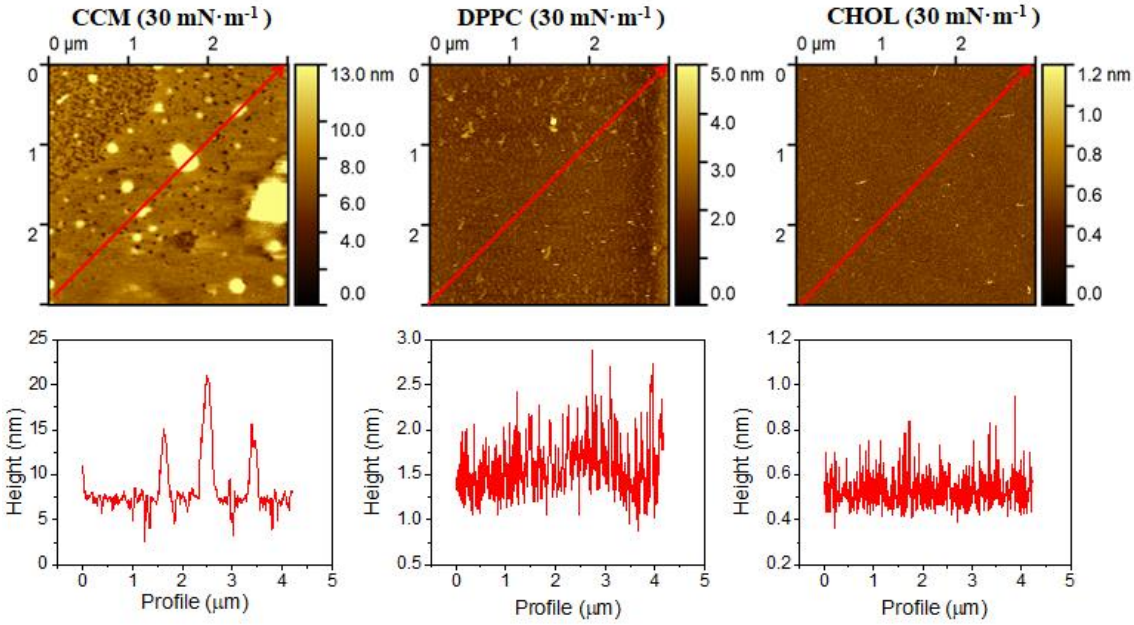

Figure 4-10. AFM images of CCM, DPPC and CHOL single monolayers at 30 $mN \cdot m^{-1}$ and their respective section profiles (red arrow).

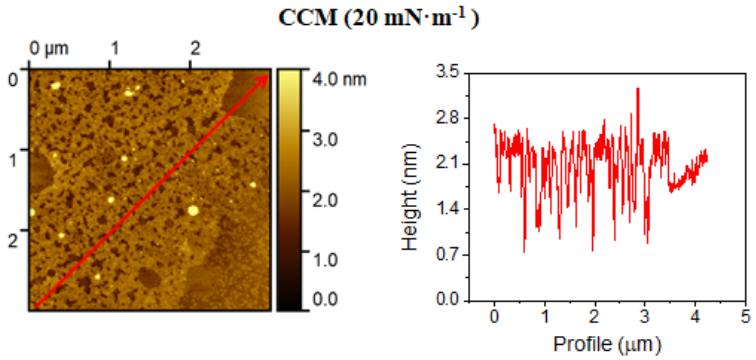

Figure 4-11. AFM image of CCM single monolayer at 20 mN·m^{-1} and its section profile (red arrow).

DPPC-CHOL binary system (**Figure 4-12**) reveals that the mixture is really homogenous (Rq-RMS roughness = 0.11 ± 0.02 nm). This supports good miscibility between DPPC and CHOL at 1:1 molar fraction, present in Eucaryotic cells. For the CCM-DPPC binary system (**Figure 4-13**), at low molar fractions of CCM the characteristic domain boundaries are significant (ca. 0.6 nm in height). As the molar fraction increases, the geometrical patterns broaden until they become indistinguishable. This suggests that the addition of CCM modifies the phases and transition phases of DPPC, thus there exists interaction between the components. This is in good agreement with the thermodynamic results for the binary systems seen in section **4.2. Binary monolayers**. In addition, 3D structures of variable height are present, and at x_{CCM} = 0.7 it is observed that the tip of the cantilever presents higher adherence with the surface; this suggests that CCM was expelled out the monolayer of DPPC, soften the surface. With respect to the CCM-CHOL binary system (**Figure 4-13**), 3D structures are present at low molar fractions of CCM. Nonetheless, for CCM-CHOL 1:1 the roughness value is quite similar to CHOL single monolayer roughness value (Rq-RMS roughness = 0.06 ± 0.01 nm). At x_{CCM} = 0.8, the roughness increases (Rq-RMS roughness = 0.25 ± 0.02 nm), but the surface seems to be more homogeneous (height median = 1.75 ± 0.01 nm).

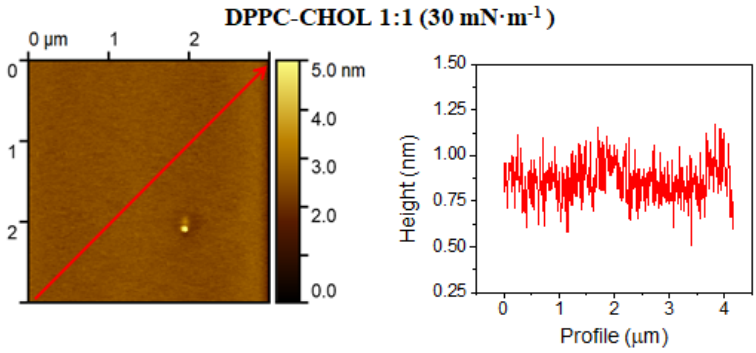

Figure 4-12. AFM image of DPPC-CHOL 1:1 binary monolayer at 30 mN·m^{-1} and its section profile (red arrow).

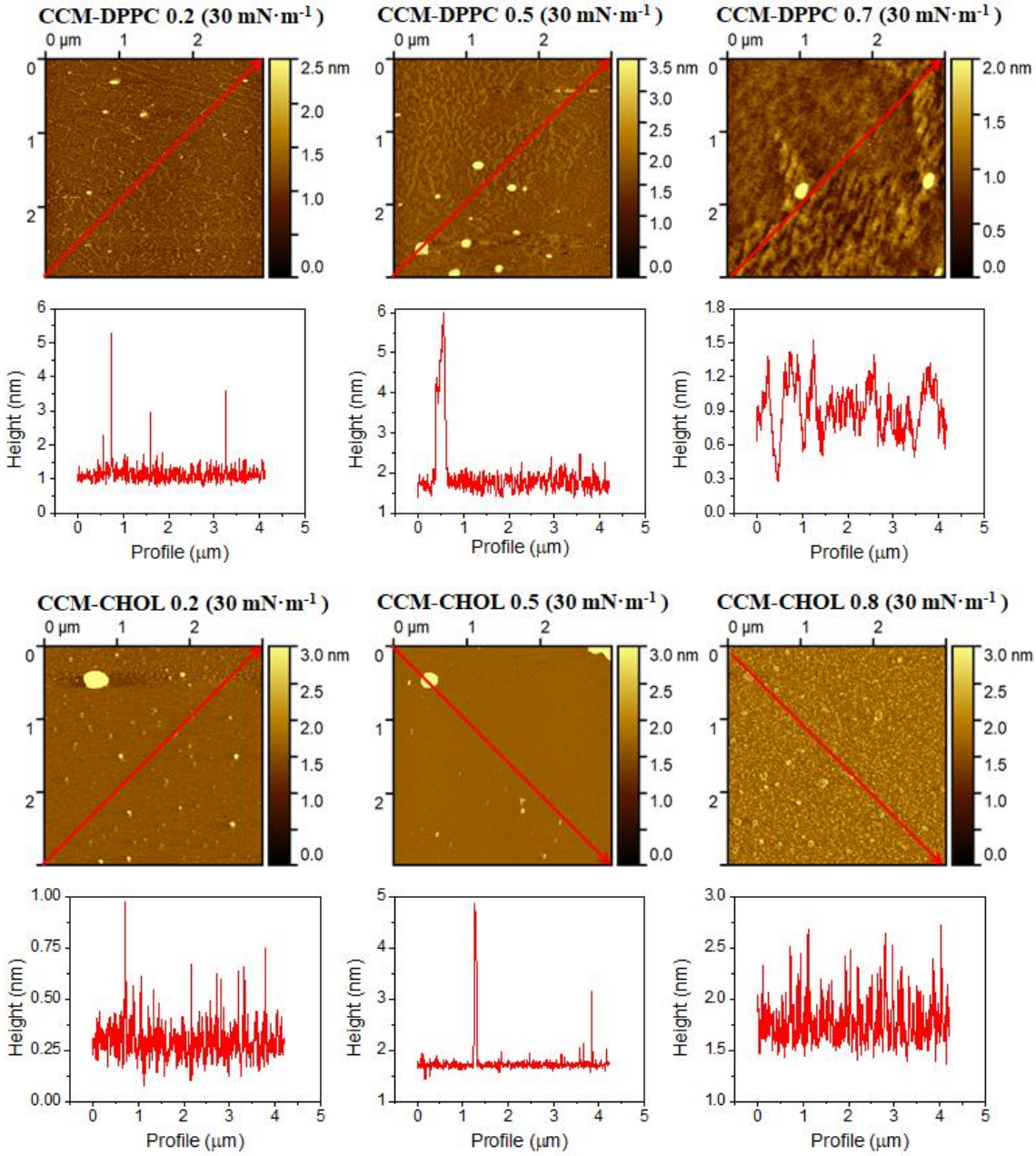

Figure 4-13. AFM images of CCM-DPPC and CCM-CHOL binary monolayers at 30 mN·m^{-1} and their respective section profiles (red arrow).

To finish, ternary LB films of x_{CCM} = 0.2, 0.33, 0.6 and 0.8, maintaining constant the molar fraction of DPPC-CHOL (1:1) are shown in **Figure 4-14**. At low molar fraction of CCM, monolayers are planar and very homogeneous, with very few 3D structures (Rq-RMS roughness = 0.10 ± 0.01 nm). As the molar fraction of CCM increases, some platforms appear (ca. 0.6-1 nm of height). This can suggest that CCM is not well mixed with the other components, but that it is expelled out of the monolayer, which may explain the slightly positive values of A^E seen before. At high molar fraction of CCM, several 3D structures are observed (ca. 10 nm in height). Comparing the 1:1:1

ternary system at 30 $mN \cdot m^{-1}$ and 20 $mN \cdot m^{-1}$, at lower surface pressure it seems to have less aggregates. In conclusion, $x_{CCM} = 0.2$ (DPPC-CHOL 1:1) presents the best miscibility between the components. This is in good agreement with the thermodynamic results obtained in section **4.3. Ternary monolayers**.

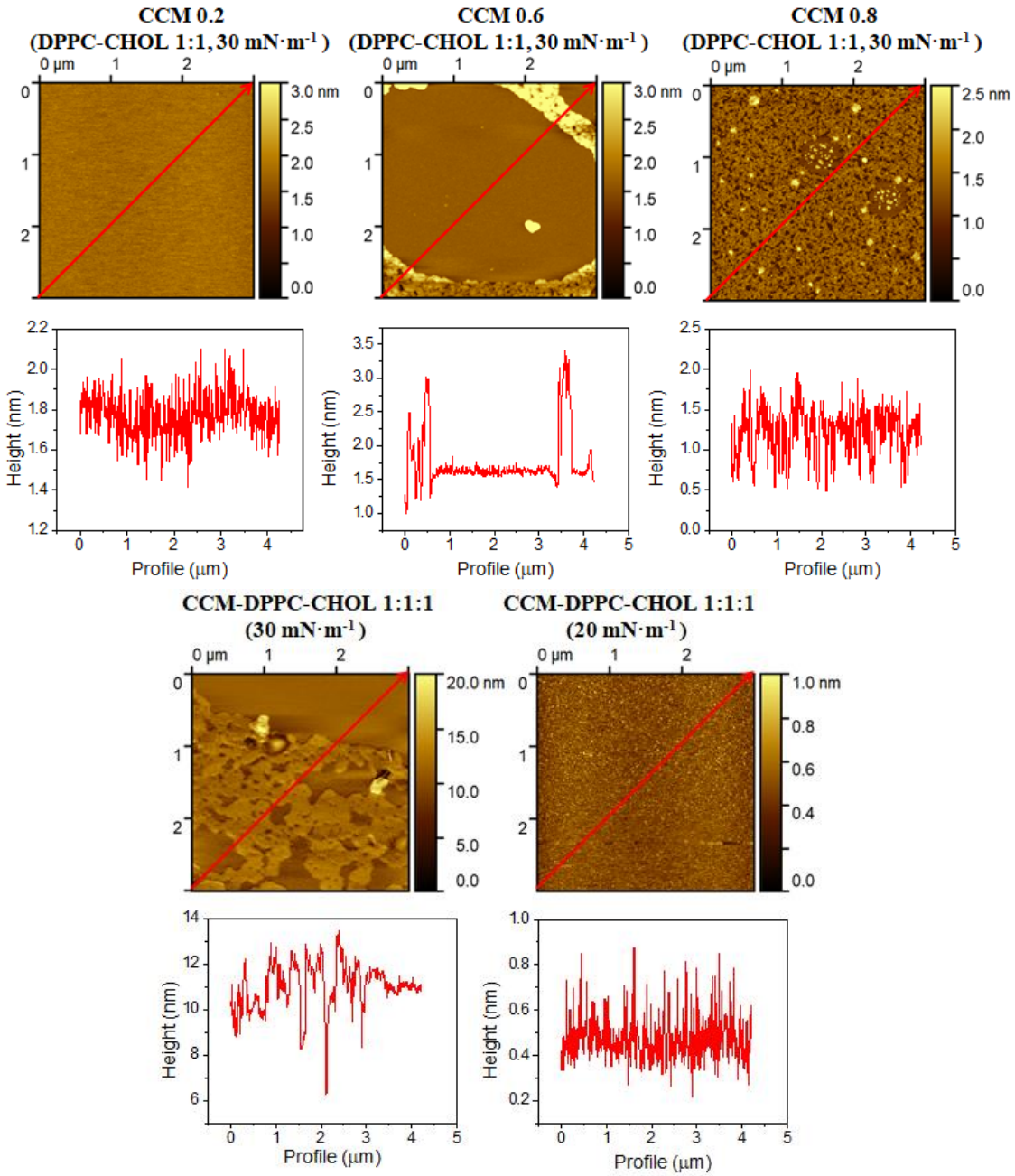

Figure 4-14. AFM images of CCM-DPPC-CHOL ternary monolayers at 30 $mN \cdot m^{-1}$ and 20 $mN \cdot m^{-1}$, and their respective section profiles (red arrow).

5 Conclusions and future prospects

This Master's Thesis stands for an innovative approach to study how CCM interacts with model cell membranes (DPPC and CHOL). The thermodynamic analysis (A^E, ${\Delta G_m}^E$, ΔG_m and Ks) is indicative of a partial miscibility between the three components. In general, the miscibility increases as the surface pressure increases, i.e. as the monolayer is more condensed. The addition of CCM implies more expanded phases as compared to those of the pure compounds, while the addition of CHOL leads to LC phases. The thermodynamic results suggest that for the A^E, the steric effect preveails, while for the ${\Delta G_m}^E$ and ΔG_m the energetic effect prevails. For both CCM-DPPC and CCM-CHOL binary monolayers, the most favourable mixture is $x_{CCM} = 0.8$. However, it is observed that the addition of CCM to DPPC destabilizes the monolayer until the CCM collapses and it is expelled out of the monolayer. On the other hand, for the DPPC-CHOL binary monolayers, the most favourable mixture is $x_{DPPC} = 0.6$. With respect to the ternary monolayers, the most favourable mixtures, at 40 $mN \cdot m^{-1}$, are x_{CCM}-x_{DPPC}-x_{CHOL} = 0.7-0.1-0.2 and 0.4-0.4-0.2 in terms of the steric effect, while in terms of the energetic effect the most favourable mixtures are x_{CCM}-x_{DPPC}-x_{CHOL} = 0.4-0.2-0.4 and 0.2-0.3-0.5, i.e. regions rich in CHOL and low molar fraction of CCM. Taken into account that the Eucaryotic cells contain DPPC-CHOL 1:1 and that the biological surface pressure is about 30 $mN \cdot m^{-1}$, the most stable monolayer is x_{CCM}-x_{DPPC}-x_{CHOL} = 0.2-0.4-0.4. AFM images support these results. Consequently, the scientific objective of this Master's Thesis has been achieved, as well as the academic objectives.

The next step in this study is the characterization of the films by other techniques, such as Raman spectroscopy and IR combined with AFM in order to obtain compositional information at the same time the topography is inspected. Also, other phospholipids can be proposed to mimic the cell membrane and other compounds such as proteins and carbohydrates can be introduced. Finally, other curcumin-nanoformulations (vesicles and micelles) can be fabricated.

References

(1) Li, X.; Mohammadi, A. S.; Ewing, A. G. Single Cell Amperometry Reveals Curcuminoids Modulate the Release of Neurotransmitters during Exocytosis from PC12 Cells. *J. Electroanal. Chem.* **2016**, *781*, 30–35. https://doi.org/https://doi.org/10.1016/j.jelechem.2016.10.025.

(2) Anand, P.; Thomas, S. G.; Kunnumakkara, A. B.; Sundaram, C.; Harikumar, K. B.; Sung, B.; Tharakan, S. T.; Misra, K.; Priyadarsini, I. K.; Rajasekharan, K. N.; Aggarwal, B. B. Biological Activities of Curcumin and Its Analogues (Congeners) Made by Man and Mother Nature. *Biochem. Pharmacol.* **2008**, *76* (11), 1590–1611. https://doi.org/10.1016/j.bcp.2008.08.008.

(3) Naksuriya, O.; Okonogi, S.; Schiffelers, R. M.; Hennink, W. E. Curcumin Nanoformulations: A Review of Pharmaceutical Properties and Preclinical Studies and Clinical Data Related to Cancer Treatment. *Biomaterials* **2014**, *35* (10), 3365–3383. https://doi.org/10.1016/j.biomaterials.2013.12.090.

(4) Yallapu, M. M.; Jaggi, M.; Chauhan, S. C. Curcumin Nanoformulations: A Future Nanomedicine for Cancer. *Drug Discov Today* **2012**, *17* (1–2), 71–81. https://doi.org/10.1016/j.drudis.2011.09.009.Curcumin.

(5) Feng, Y.; Wang, N.; Cheung, F.; Zhu, M.; Li, H.; Feng, Y. Molecular and Celluar Mechanism Studies on Anticancer Effects of Chinese Medicines. *Biomed. Eng. Trends, Res. Technol.* **2011**, No. June 2014. https://doi.org/10.5772/13613.

(6) J. González-Albadalejo; Dionisia Sanz; Rosa M. Claramunt; José Luis Lavandera; Ibon Alkorta; José Elguero. Curcumin and Curcuminoids: Chemistry, Structural Studies and Biological Properties. *An. la Real Acad. Nac. Farm.* **2015**, *81* (4), 278–310.

(7) DrugBanck. "Curcumin". https://go.drugbank.com/drugs/DB11672 (accessed May 11, 2021).

(8) Alberts, B. *Molecular Biology of the Cell*; 2015.

(9) Siontorou, C. G.; Nikoleli, G. P.; Nikolelis, D. P.; Karapetis, S. K. Artificial Lipid Membranes: Past, Present, and Future. *Membranes*. MDPI AG September 1, 2017. https://doi.org/10.3390/membranes7030038.

(10) Ruiz-Rincón, S.; González-Orive, A.; De La Fuente, J. M.; Cea, P. Reversible Monolayer-Bilayer Transition in Supported Phospholipid LB Films under the Presence of Water: Morphological and Nanomechanical Behavior. *Langmuir* **2017**, *33* (30), 7538–7547. https://doi.org/10.1021/acs.langmuir.7b01268.

(11) Toimil, P.; Prieto, G.; Miñones, J.; Sarmiento, F. A Comparative Study of F-DPPC/DPPC Mixed Monolayers. Influence of Subphase Temperature on F-DPPC and DPPC Monolayers. *Phys. Chem. Chem. Phys.* **2010**, *12* (40), 13323–13332. https://doi.org/10.1039/c0cp00506a.

(12) Krause, M. R.; Regen, S. L. The Structural Role of Cholesterol in Cell Membranes: From Condensed Bilayers to Lipid Rafts. *Acc. Chem. Res.* **2014**, *47* (12), 3512–3521. https://doi.org/10.1021/ar500260t.

(13) Web of Science (WOS). "Curcumin". https://wcs.webofknowledge.com/RA/analyze.do?product=UA&SID=D3AInvmYCQenQpKwk55&field=SJ_ResearchArea_ResearchArea_en&yearSort=false (accessed Apr 16, 2021).

(14) Cheng, C.; Peng, S.; Li, Z.; Zou, L.; Liu, W.; Liu, C. Improved Bioavailability of Curcumin in Liposomes Prepared Using a PH-Driven, Organic Solvent-Free, Easily Scalable Process. *RSC Adv.* **2017**, *7* (42), 25978–25986. https://doi.org/10.1039/c7ra02861j.

(15) Moussa, Z.; Chebl, M.; Patra, D. Interaction of Curcumin with 1,2-Dioctadecanoyl-Sn-Glycero-3-Phosphocholine Liposomes: Intercalation of Rhamnolipids Enhances Membrane Fluidity, Permeability and Stability of Drug Molecule. *Colloids Surfaces B Biointerfaces* **2017**, *149*, 30–37. https://doi.org/10.1016/j.colsurfb.2016.10.002.

(16) Narayanan, N. K.; Nargi, D.; Randolph, C.; Narayanan, B. A. Liposome Encapsulation of Curcumin and Resveratrol in Combination Reduces Prostate Cancer Incidence in PTEN Knockout Mice. *Int. J. Cancer* **2009**, *125* (1), 1–8. https://doi.org/10.1002/ijc.24336.

(17) Mondal, S.; Ghosh, S.; Moulik, S. P. Colloidal Dispersions of Lipids and Curcumin, and the Solubility and Degradation Kinetics of the Latter in Micellar Solution. *Soft Mater.* **2015**, *13* (2),

118–125. https://doi.org/10.1080/1539445X.2015.1025981.

(18) Kotenkov, S. A.; Gnezdilov, O. I.; Khaliullina, A. V.; Antzutkin, O. N.; Gimatdinov, R. S.; Filippov, A. V. Effect of Cholesterol and Curcumin on Ordering of DMPC Bilayers. *Appl. Magn. Reson.* **2019**, *50* (1–3), 511–520. https://doi.org/10.1007/s00723-018-1102-2.

(19) Filippov, A. V.; Kotenkov, S. A.; Munavirov, B. V.; Khaliullina, A. V.; Gnezdilov, O. I.; Antzutkin, O. N. Effect of Curcumin on Lateral Diffusion in Lipid Bilayers. *Mendeleev Commun.* **2016**, *26* (2), 109–110. https://doi.org/10.1016/j.mencom.2016.03.007.

(20) Ausili, A.; Gómez-Murcia, V.; Candel, A. M.; Beltrán, A.; Torrecillas, A.; He, L.; Jiang, Y.; Zhang, S.; Teruel, J. A.; Gómez-Fernández, J. C. A Comparison of the Location in Membranes of Curcumin and Curcumin-Derived Bivalent Compounds with Potential Neuroprotective Capacity for Alzheimer's Disease. *Colloids Surfaces B Biointerfaces* **2021**, *199* (December 2020). https://doi.org/10.1016/j.colsurfb.2020.111525.

(21) Gardikis, K.; Hatziantoniou, S.; Viras, K.; Demetzos, C. Effect of a Bioactive Curcumin Derivative on DPPC Membrane: A DSC and Raman Spectroscopy Study. *Thermochim. Acta* **2006**, *447* (1), 1–4. https://doi.org/10.1016/j.tca.2006.03.007.

(22) El Khoury, E.; Patra, D. Length of Hydrocarbon Chain Influences Location of Curcumin in Liposomes: Curcumin as a Molecular Probe to Study Ethanol Induced Interdigitation of Liposomes. *J. Photochem. Photobiol. B Biol.* **2016**, *158*, 49–54. https://doi.org/10.1016/j.jphotobiol.2016.02.022.

(23) Jalili, S.; Saeedi, M. Study of Curcumin Behavior in Two Different Lipid Bilayer Models of Liposomal Curcumin Using Molecular Dynamics Simulation. *J. Biomol. Struct. Dyn.* **2016**, *34* (2), 327–340. https://doi.org/10.1080/07391102.2015.1030692.

(24) Girardon, M.; Korchowiec, B.; Korchowiec, J.; Rogalska, E.; Canilho, N.; Pasc, A. A Way to Introducing a Hydrophilic Bioactive Agent into Model Lipid Membranes. The Role of Cetyl Palmitate in the Interaction of Curcumin with 1,2-Dioleoyl-Sn-Glycero-3-Phosphatidylcholine Monolayers. *J. Mol. Liq.* **2020**, *308*, 113040. https://doi.org/10.1016/j.molliq.2020.113040.

(25) Peng, Q.; Zeng, C.; Zhou, Y.; Lian, S.; Nie, G. Rapid Determination of Turmeric Roots Quality Based on the Raman Spectrum of Curcumin. *Food Anal. Methods* **2015**, *8* (1), 103–108. https://doi.org/10.1007/s12161-014-9874-y.

(26) Niu, Y.; Wang, X.; Chai, S.; Chen, Z.; An, X.; Shen, W. Effects of Curcumin Concentration and Temperature on the Spectroscopic Properties of Liposomal Curcumin. *J. Agric. Food Chem.* **2012**, *60* (7), 1865–1870. https://doi.org/10.1021/jf204867v.

(27) Castillo, M. L. R. Del; López-Tobar, E.; Sanchez-Cortes, S.; Flores, G.; Blanch, G. P. Stabilization of Curcumin against Photodegradation by Encapsulation in Gamma-Cyclodextrin: A Study Based on Chromatographic and Spectroscopic (Raman and UV-Visible) Data. *Vib. Spectrosc.* **2015**, *81*, 106–111. https://doi.org/10.1016/j.vibspec.2015.10.008.

(28) Benassi, R.; Ferrari, E.; Lazzari, S.; Spagnolo, F.; Saladini, M. Theoretical Study on Curcumin: A Comparison of Calculated Spectroscopic Properties with NMR, UV-Vis and IR Experimental Data. *J. Mol. Struct.* **2008**, *892* (1–3), 168–176. https://doi.org/10.1016/j.molstruc.2008.05.024.

(29) Priyadarsini, K. I. The Chemistry of Curcumin: From Extraction to Therapeutic Agent. *Molecules* **2014**, *19* (12), 20091–20112. https://doi.org/10.3390/molecules191220091.

(30) Kolev, T. M.; Velcheva, E. A.; Stamboliyska, B. A.; Spiteller, M. DFT and Experimental Studies of the Structure and Vibrational Spectra of Curcumin. *Int. J. Quantum Chem.* **2005**, *102* (6), 1069–1079. https://doi.org/10.1002/qua.20469.

(31) Leite, N. B.; Martins, D. B.; Fazani, V. E.; Vieira, M. R.; dos Santos Cabrera, M. P. Cholesterol Modulates Curcumin Partitioning and Membrane Effects. *Biochim. Biophys. Acta - Biomembr.* **2018**, *1860* (11), 2320–2328. https://doi.org/10.1016/j.bbamem.2018.05.018.

(32) Chignell, C. F.; Bilski, P.; Reszka, K. J.; Motten, A. G.; Sik, R. H.; Dahl, T. A. Spectral and Photochemical Properties of Curcumin. *Photochem. Photobiol.* **1994**, *59* (3), 295–302. https://doi.org/10.1111/j.1751-1097.1994.tb05037.x.

(33) Xu, G.; Hao, C.; Zhang, L.; Sun, R. Investigation of Surface Behavior of DPPC and Curcumin in Langmuir Monolayers at the Air-Water Interface. *Scanning* **2017**, *2017*.

https://doi.org/10.1155/2017/6582019.

(34) Karewicz, A.; Bielska, D.; Gzyl-Malcher, B.; Kepczynski, M.; Lach, R.; Nowakowska, M. Interaction of Curcumin with Lipid Monolayers and Liposomal Bilayers. *Colloids Surfaces B Biointerfaces* **2011**, *88* (1), 231–239. https://doi.org/10.1016/j.colsurfb.2011.06.037.

(35) Langmuir, I. The Constitution and Fundamental Properties of Solids and Liquids. II Liquids. *J. Am. Chem. Soc.* **1917**, *39* (9), 1848–1906. https://doi.org/10.1021/ja02254a006.

(36) Davies, J. T.; Rideal, E. K. *Interfacial Phenomena*; Academic Press: New York, 1963.

(37) Adamson, A. W.; Gast, A. P. *Physical Chemistry of Surfaces*, Sixth.; Whiler: New York, 1997.

(38) Crisp, D. J. *Surface Phenomena in Chemistry and Biology*; Danielli, J. F., Pankhurst, K. G. A., Riddiford, A. C., Eds.; Pergamon Press: London, 1958.

(39) Maget-Dana, R. *The Monolayer Technique: A Potent Tool for Studying the Interfacial Properties of Antimicrobial and Membrane-Lytic Peptides and Their Interactions with Lipid Membranes*; 1999; Vol. 1462. https://doi.org/10.1016/S0005-2736(99)00203-5.

(40) Zsako, J.; Tomoaia-Cotişel, M.; Chifu, E. Insoluble Mixed Monolayers. I. Phase Equilibria at the Collapse of Binary Monolayers at Gas/Liquid Interfaces. *J. Colloid Interface Sci.* **1984**, *102* (1), 186–205. https://doi.org/10.1016/0021-9797(84)90212-1.

(41) Chattoraj, D. *Adsorption and the Gibbs Surface Excess*; Plenum Press: New York and London, 1984. https://doi.org/10.1007/978-4615-8333-2.

(42) Meyer, E.; Hug, H. J.; Bennewitz, R. *Scanning Probe Microscopy: The Lab on a Tip.*, First.; Springer-Verlag Berlin Heidelberg, 2004. https://doi.org/10.1007/978-3-662-09801-1.

(43) Vist, M. R.; Davis, J. H. Phase Equilibria of Cholesterol/Dipalmitoylphosphatidylcholine Mixtures: 2H Nuclear Magnetic Resonance and Differential Scanning Calorimetry. *Biochemistry* **1990**, *29* (2), 451–464. https://doi.org/10.1021/bi00454a021.

(44) Miyoshi, T.; Kato, S. Detailed Analysis of the Surface Area and Elasticity in the Saturated 1,2-Diacylphosphatidylcholine/Cholesterol Binary Monolayer System. *Langmuir* **2015**, *31* (33), 9086–9096. https://doi.org/10.1021/acs.langmuir.5b01775.

(45) Hung, W. C.; Lee, M. T.; Chen, F. Y.; Huang, H. W. The Condensing Effect of Cholesterol in Lipid Bilayers. *Biophys. J.* **2007**, *92* (11), 3960–3967. https://doi.org/10.1529/biophysj.106.099234.

(46) Róg, T.; Pasenkiewicz-Gierula, M.; Vattulainen, I.; Karttunen, M. Ordering Effects of Cholesterol and Its Analogues. *Biochim. Biophys. Acta - Biomembr.* **2009**, *1788* (1), 97–121. https://doi.org/10.1016/j.bbamem.2008.08.022.

(47) Reis, O.; Winter, R.; Zerda, T. W. The Effect of High External Pressure on DPPC-Cholesterol Multilamellar Vesicles: A Pressure-Tuning Fourier Transform Infrared Spectroscopy Study. *Biochim. Biophys. Acta - Biomembr.* **1996**, *1279* (1), 5–16. https://doi.org/10.1016/0005-2736(95)00233-2.

(48) Chapman, D. Phospholipid Bilayers Physical Principles and Models. Gregor Cevc and Derek Marsh (Eds), John Wiley and Sons Ltd. Xvi + 442 Pages, £73.35 (1987). *Cell Biochem. Funct.* **1988**, *6* (2), 147–148. https://doi.org/https://doi.org/10.1002/cbf.290060221.

(49) Oncins, G.; Picas, L.; Hernández-Borrell, J.; Garcia-Manyes, S.; Sanz, F. Thermal Response of Langmuir-Blodgett Films of Dipalmitoylphosphatidylcholine Studied by Atomic Force Microscopy and Force Spectroscopy. *Biophys. J.* **2007**, *93* (8), 2713–2725. https://doi.org/10.1529/biophysj.107.110916.

ANEXES

1 ANNEX I

In the following table, chemical and physical properties of CCM, DPPC and CHOL are further described (data collected from PubChem databases).

	Curcumin	**DPPC**	**Cholesterol**
Formula	$C_{21}H_{20}O_6$	$C_{40}H_{80}NO_8P$	$C_{27}H_{46}O$
MW ($g \cdot mol^{-1}$)	368.4	734.0	386.7
Appearance	Yellow-orange crystalline solid	White crystalline solid	White or faintly yellow pearly granules or crystals
Solubility	Insoluble in water. Soluble in organic solvents (alcohols, chloroform)	Very poor solubility in water. Soluble in organic solvents (chloroform).	Poor solubility in water. Moderately soluble in hot alcohol; soluble in benzene, oils, fats and aqueous solutions of bile salts.
Stability	Stable at acid pH and RT.	Stable. Incompatible with strong oxidizing agents.	Stable.
Structure	β dicetone α-β unsaturated, p-phenolic rings, high conjugation symmetric, without stereogenic centres. Polymorphism. Ceto-enol tautomery (the enolic form predominates both in aqueous and organic solvents)	Lipid. Phosphatidylcholine 32:0, 1-acyl-2-hexadecanoyl-sn-glycero-3-phosphocholine, derives from a hexadecanoic acid.	Sterol (lipid). Sterane (cyclopentanoper-hydrophenanthrenes). Hydroxyl group, C_3. 8 stereocenters→256 stereoisomers, although only two are of biochemical significance (*nat*-cholesterol and *ent*-cholesterol).
H bond acceptors	6 atoms	8 atoms	1 atom
H bond donors	2 atoms	0 atoms	1 atom
Rotatable bonds	8 bonds	40 bonds	5 bonds
Formal charge	0	0	0
Others	Photosensibility. Fluorescence. Amphipathic behaviour: polarity in the center of the molecule and the adjacent groups, so it can interact with proteins and lipids of biologic membranes.	Lung surfactant. Amphipathic behaviour: hydrophilic head, composed of the polar phosphatidylcholine group, and hydrophobic tails, formed by two nonpolar palmitic acid (C_{16}) chains. Formation of micelles, monolayers, bilayers and liposomes in polar solvents.	Specific rotation: -34º to 38º at 25 °C. The hydroxyl group interacts with water molecules and the polar heads of phospholipids while the bulky steroid is embedded in the membrane, alongside the nonpolar fatty-acid chains.
Hazards	H304: aspiration hazard H317: sensitization, allergic skin reaction H412: hazardous to the aquatic environment, long-term hazard Not flammable or combustible.	Not Classified	Not Classified

2 ANNEX II

In the following figure and table, the molar fraction experiments for binary and ternary systems are shown.

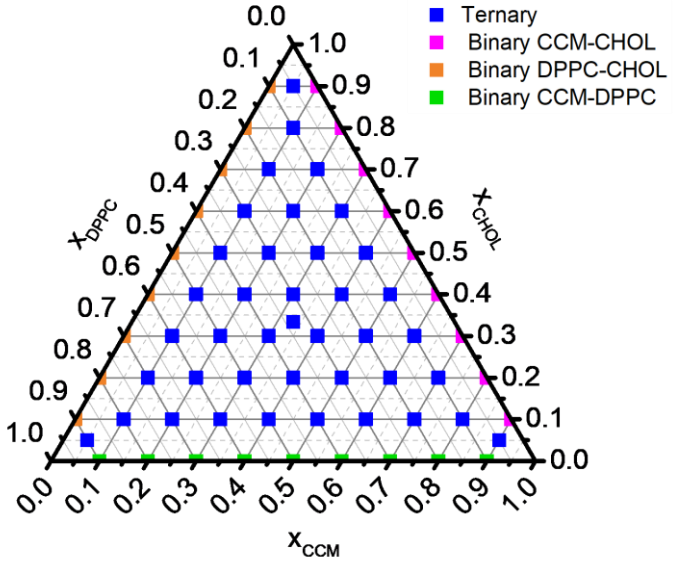

Figure 2-1. Graphic representation of the binary and ternary systems in a ternary diagram.

Table 2-1. Composition of the binary and ternary systems.

TERNARY SYSTEMS				BINARY SYSTEMS		
Number	**x_{CCM}**	**x_{CHOL}**	**x_{DPPC}**	**Number**	**x_{CCM}**	**x_{CHOL}**
1	0.9	0.05	0.05	**1**	0.1	0.9
2	0.8	0.1	0.1	**2**	0.2	0.8
3	0.7	0.1	0.2	**3**	0.3	0.7
4	0.7	0.2	0.1	**4**	0.4	0.6
5	0.6	0.1	0.3	**5**	0.5	0.5
6	0.6	0.2	0.2	**6**	0.6	0.4
7	0.6	0.3	0.1	**7**	0.7	0.3
8	0.5	0.1	0.4	**8**	0.8	0.2
9	0.5	0.2	0.3	**9**	0.9	0.1
10	0.5	0.3	0.2	**Number**	**x_{CCM}**	**x_{DPPC}**
11	0.5	0.4	0.1	**1**	0.1	0.9
12	0.4	0.1	0.5	**2**	0.2	0.8
13	0.4	0.2	0.4	**3**	0.3	0.7
14	0.4	0.3	0.3	**4**	0.4	0.6
15	0.4	0.4	0.2	**5**	0.5	0.5
16	0.4	0.5	0.1	**6**	0.6	0.4
17	0.3	0.1	0.6	**7**	0.7	0.3
18	0.3	0.2	0.5	**8**	0.8	0.2
19	0.3	0.3	0.4	**9**	0.9	0.1

TERNARY SYSTEMS				BINARY SYSTEMS		
Number	**x_{CCM}**	**x_{CHOL}**	**x_{DPPC}**	**Number**	**X_{DPPC}**	**x_{CHOL}**
20	0.3	0.4	0.3	**1**	0.1	0.9
21	0.3	0.5	0.2	**2**	0.2	0.8
22	0.3	0.6	0.1	**3**	0.3	0.7
23	0.2	0.1	0.7	**4**	0.4	0.6
24	0.2	0.2	0.6	**5**	0.5	0.5
25	0.2	0.3	0.5	**6**	0.6	0.4
26	0.2	0.4	0.4	**7**	0.7	0.3
27	0.2	0.5	0.3	**8**	0.8	0.2
28	0.2	0.6	0.2	**9**	0.9	0.1
29	0.2	0.7	0.1	**9**	0.9	0.1
30	0.1	0.1	0.8			
31	0.1	0.2	0.7			
32	0.1	0.3	0.6			
33	0.1	0.4	0.5			
34	0.1	0.5	0.4			
35	0.1	0.6	0.3			
36	0.1	0.7	0.2			
37	0.1	0.8	0.1			
38	0.05	0.05	0.9			
39	0.05	0.9	0.05			
40	0.33	0.33	0.33			

3 ANNEX III

In the following figures, the collapse surface pressure vs. molar fraction plots for all the binary systems are shown. The black points and lines represent the experimental values, while the coloured points and dashed lines represent the ideal values.

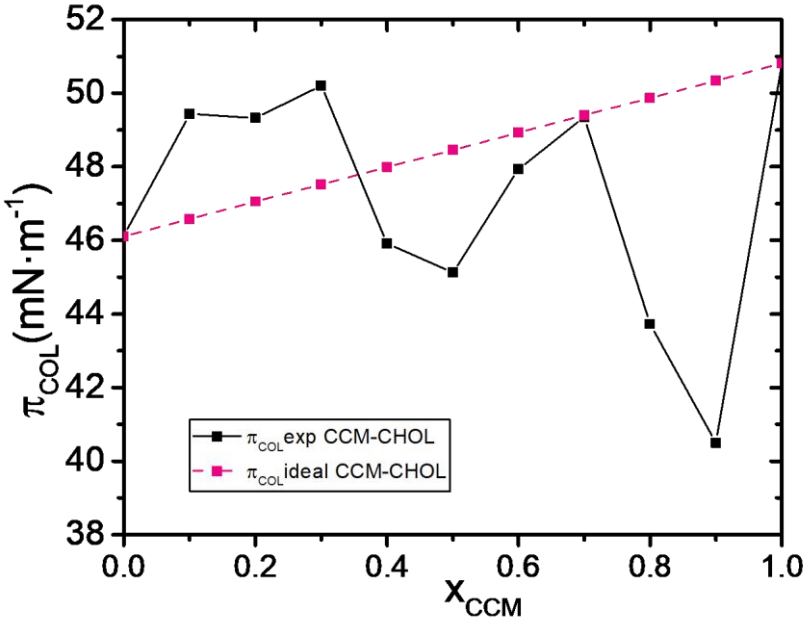

Figure 3-1. π_{COL}-x_{CCM} plot for CCM-CHOL binary monolayers at 20ºC.

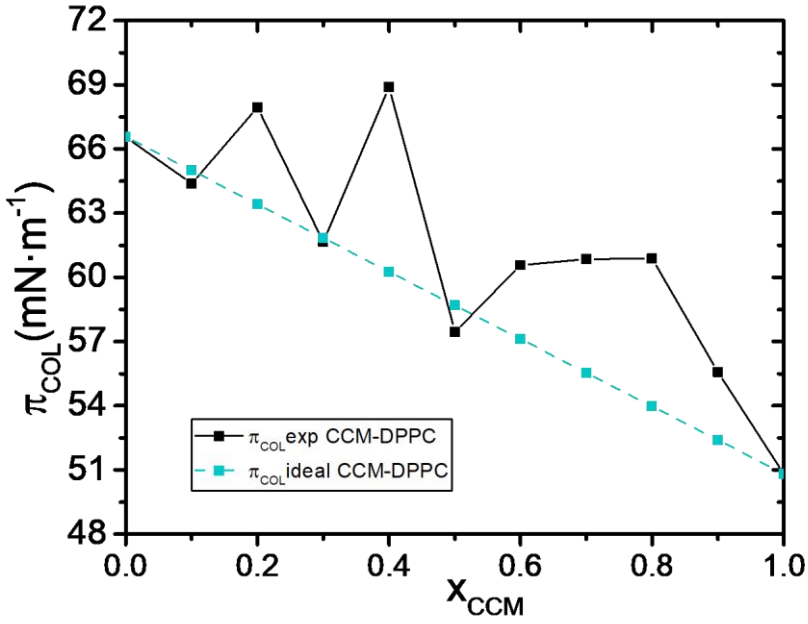

Figure 3-2. π_{COL}-x_{CCM} plot for CCM-DPPC binary monolayers at 20ºC.

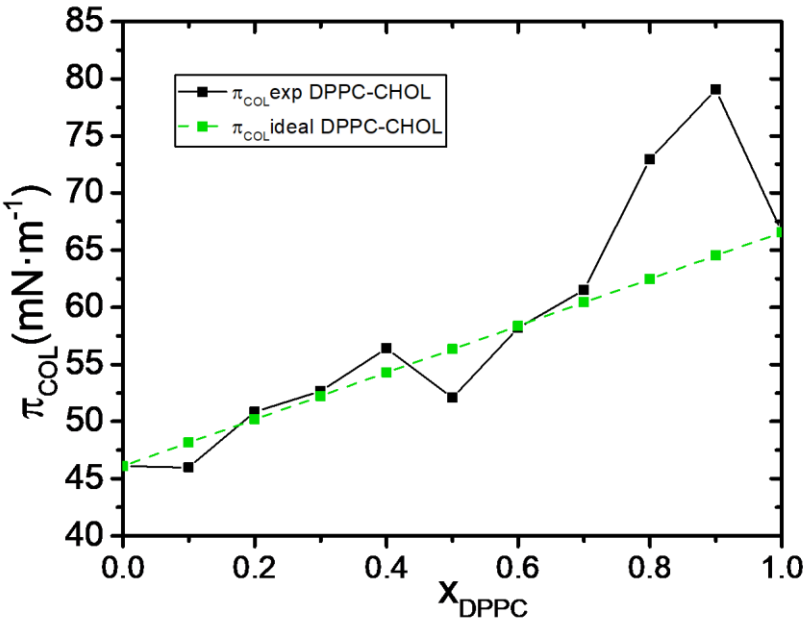

Figure 3-3. . π_{COL}-x_{DPPC} plot for DPPC-CHOL binary monolayers at 20ºC.

4 ANNEX IV

In the **Figure 4-1**, all the surface pressure-area (π-A) isotherms of the ternary systems at the different molar fractions of CCM are presented.

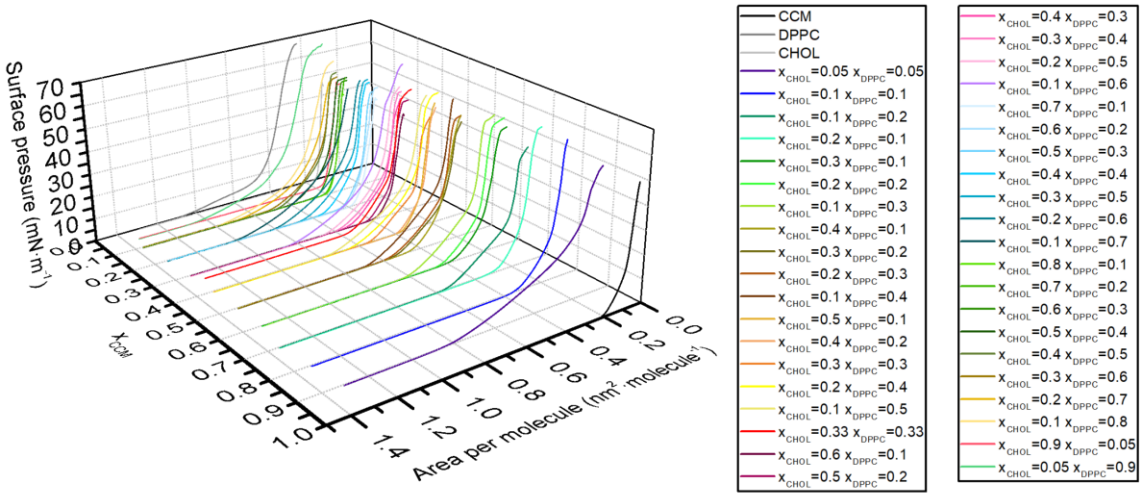

Figure 4-1. π-A isotherms for CCM-DPPC-CHOL ternary systems at different molar fractions of CCM (x, y, z = x_{CCM}, A, π)

In the following figures, the influence of CHOL and DPPC at the same CCM molar fraction is studied. On the left, detailed plots of the surface pressure-area (π-A) isotherms are presented. On the right, Ks- π plots are shown.

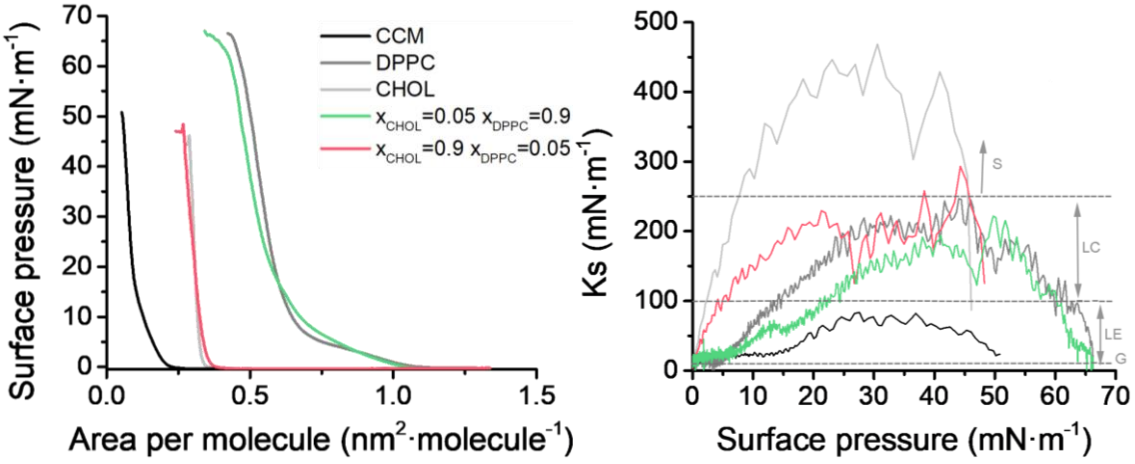

Figure 4-2. (Left) π-A isotherms for the monolayers of x_{CCM} = 0.05 ternary systems at 20ºC. (Right) Ks-π plot for the monolayers of x_{CCM} = 0.05 ternary systems.

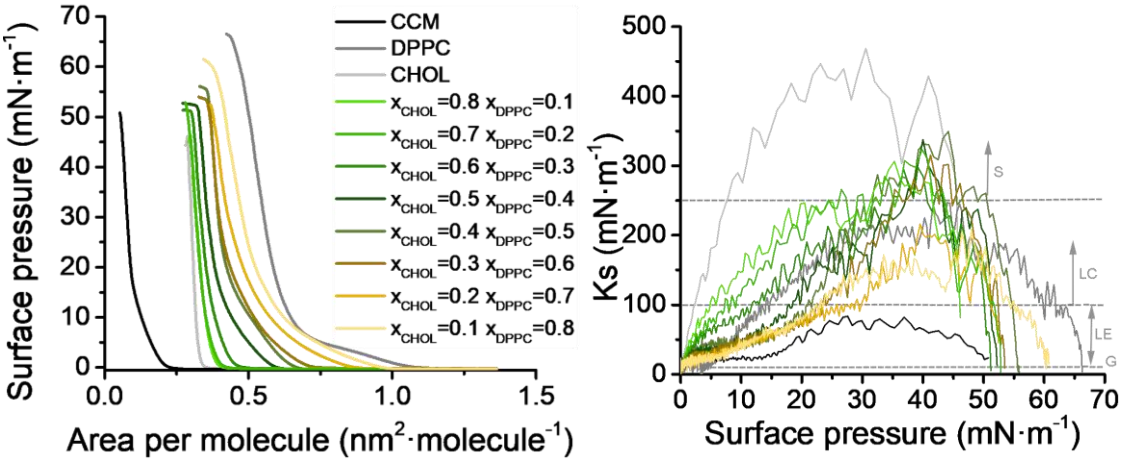

Figure 4-3. (Left) π-A isotherms for the monolayers of x_{CCM} = 0.1 ternary systems at 20°C. (Right) Ks-π plot for the monolayers of x_{CCM} = 0.1 ternary systems.

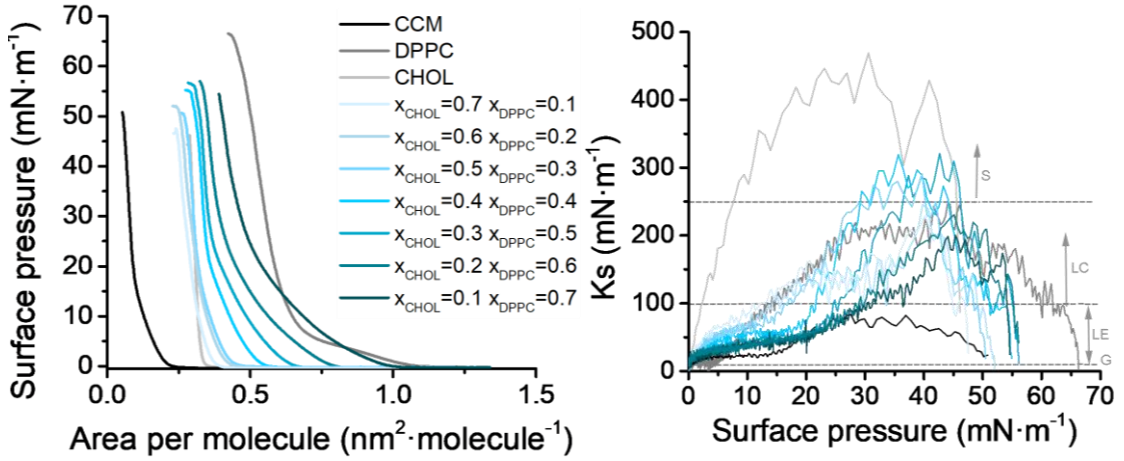

Figure 4-4. (Left) π-A isotherms for the monolayers of x_{CCM} = 0.2 ternary systems at 20°C. (Right) Ks-π plot for the monolayers of x_{CCM} = 0.2 ternary systems.

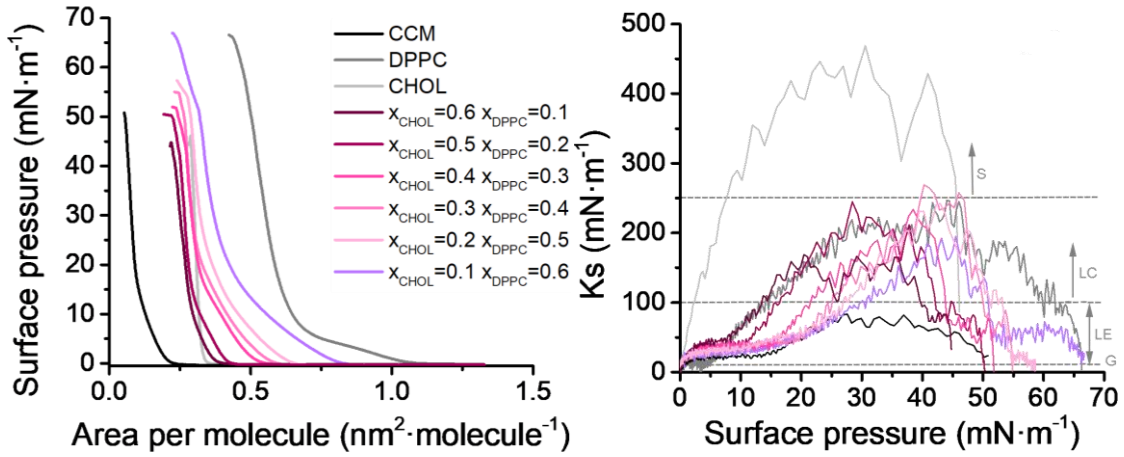

Figure 4-5. (Left) π-A isotherms for the monolayers of x_{CCM} = 0.3 ternary systems at 20°C. (Right) Ks-π plot for the monolayers of x_{CCM} = 0.3 ternary systems.

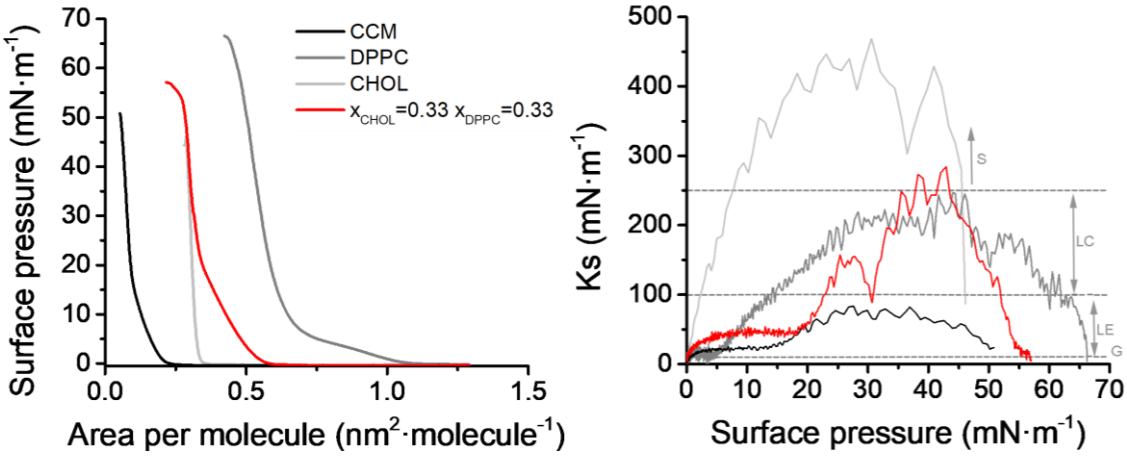

Figure 4-6. (Left) π-A isotherms for the monolayers of x_{CCM} = 0.33 ternary systems at 20°C. (Right) Ks-π plot for the monolayers of x_{CCM} = 0.33 ternary systems.

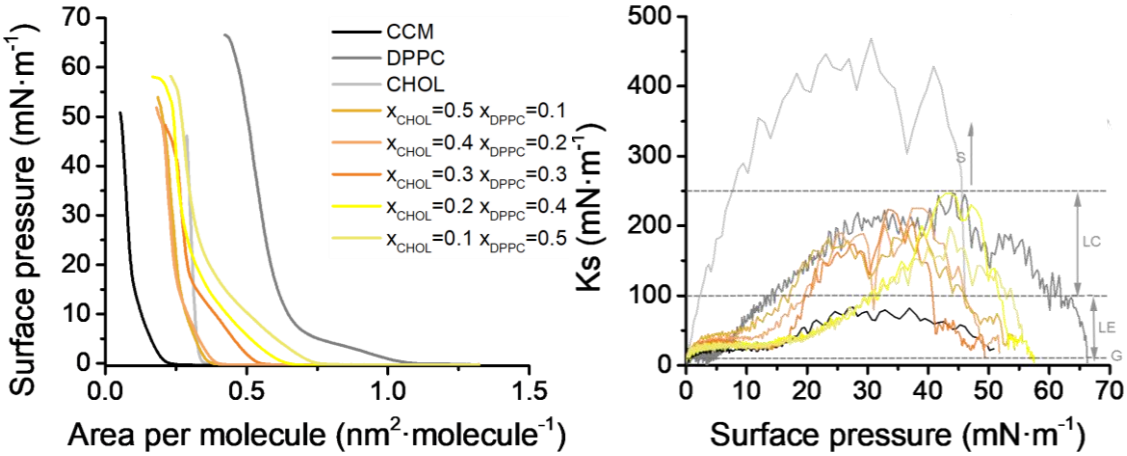

Figure 4-7. (Left) π-A isotherms for the monolayers of x_{CCM} = 0.4 ternary systems at 20°C. (Right) Ks-π plot for the monolayers of x_{CCM} = 0.4 ternary systems.

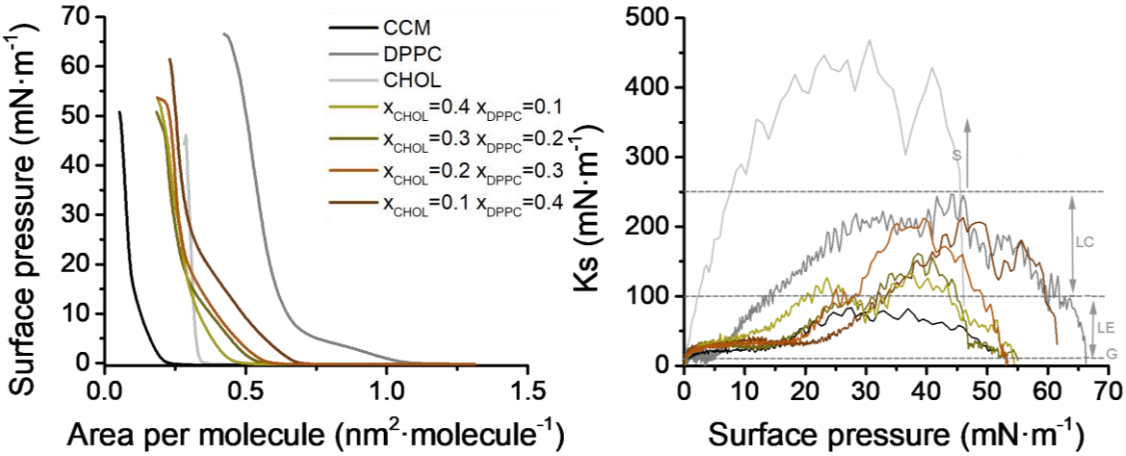

Figure 4-8. (Left) π-A isotherms for the monolayers of x_{CCM} = 0.5 ternary systems at 20°C. (Right) Ks-π plot for the monolayers of x_{CCM} = 0.5 ternary systems.

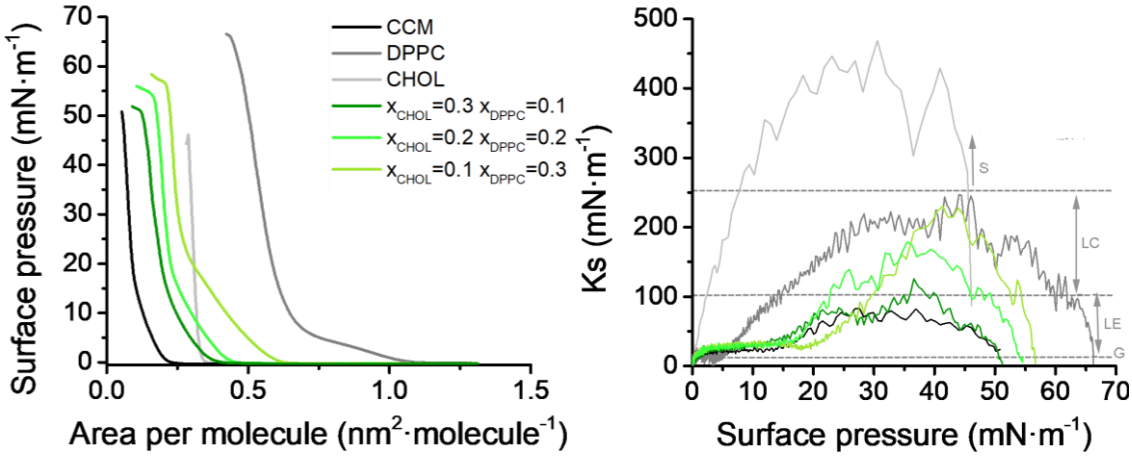

Figure 4-9. (Left) π-A isotherms for the monolayers of x_{CCM} = 0.6 ternary systems at 20ºC. (Right) Ks-π plot for the monolayers of x_{CCM} = 0.6 ternary systems.

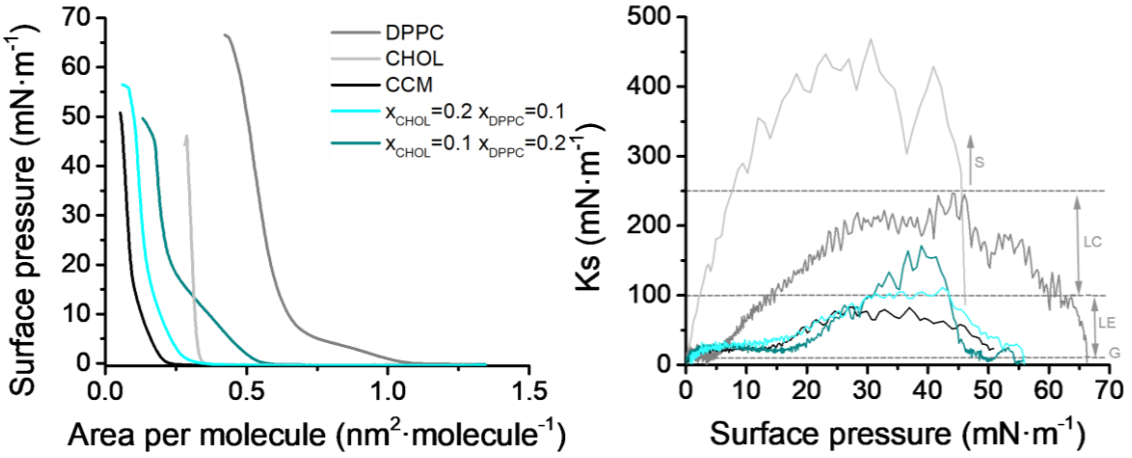

Figure 4-10. (Left) π-A isotherms for the monolayers of x_{CCM} = 0.7 ternary systems at 20ºC. (Right) Ks-π plot for the monolayers of x_{CCM} = 0.7 ternary systems.

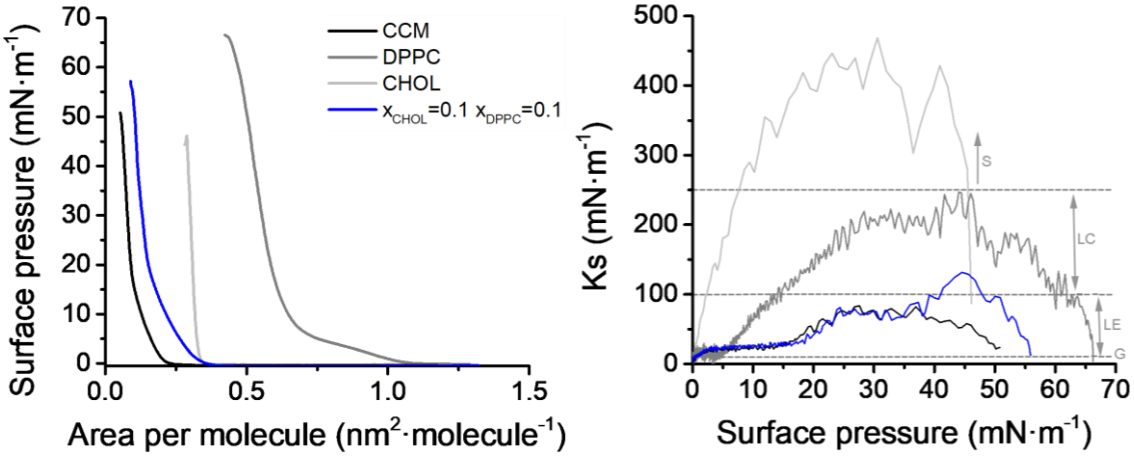

Figure 4-11. (Left) π-A isotherms for the monolayer of x_{CCM} = 0.8 ternary system at 20ºC. (Right) Ks-π plot for the monolayer of x_{CCM} = 0.8 ternary system.

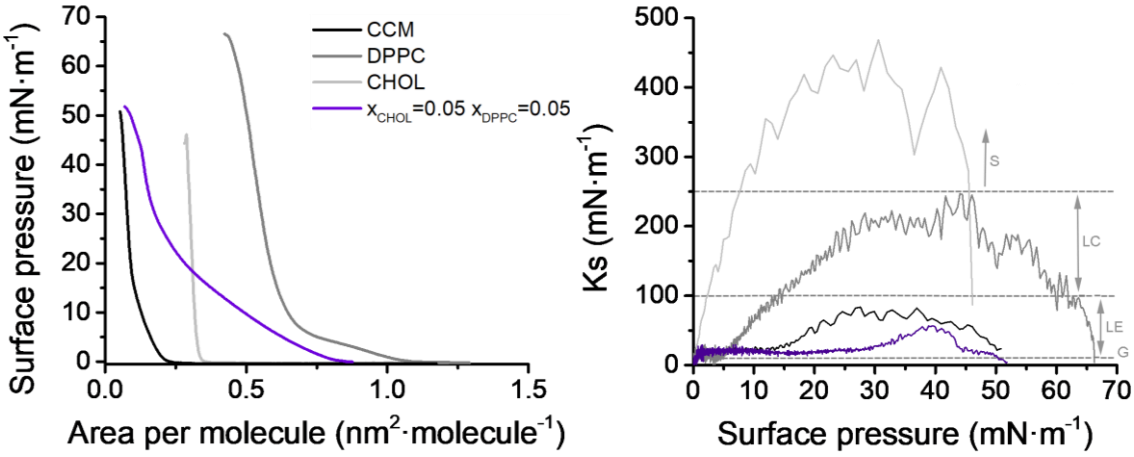

Figure 4-12. (Left) π-A isotherms for the monolayer of x_{CCM} = 0.9 ternary system at 20ºC. (Right) Ks-π plot for the monolayer of x_{CCM} = 0.9 ternary system.

5 ANNEX V

In the following tables, the thermodynamic parameters (A^E, $\Delta {G_m}^E$, ΔG_m and *Ks*) are presented for the mixtures maintaining constant the composition of DPPC-CHOL (1:1). These values are extracted from the ternary diagrams.

Table 5-1. π = 5 mN·m^{-1}

x_{CCM}	x_{CHOL}	x_{DPPC}	A^E(nm^2·molecule^{-1})	$\Delta G_M{}^E$ (J·mol^{-1})	ΔG_M (J·mol^{-1})	*Ks* (mN·m^{-1})
0	**0.5**	**0.5**	-0.0200	-186.3	-1875.7	37.0
0.2	**0.4**	**0.4**	0.0100	-70.0	-2641.1	44.6
0.33	**0.33**	**0.33**	0.0679	196.7	-2480.9	35.0
0.4	**0.3**	**0.3**	0.0655	156.8	-2497.1	35.9
0.6	**0.2**	**0.2**	0.0434	138.7	-2177.3	24.1
0.8	**0.1**	**0.1**	0.0271	73.0	-1484.5	24.2
0.9	**0.05**	**0.05**	0.4294	1606.6	645.3	24.8

Table 5-2. π = 10 mN·m^{-1}

x_{CCM}	x_{CHOL}	x_{DPPC}	A^E(nm^2·molecule^{-1})	$\Delta G_M{}^E$ (J·mol^{-1})	ΔG_M (J·mol^{-1})	*Ks* (mN·m^{-1})
0	**0.5**	**0.5**	-0.0201	-284.5	-1973.8	61.3
0.2	**0.4**	**0.4**	0.0172	-47.4	-2618.5	58.0
0.33	**0.33**	**0.33**	0.0645	372.2	-2305.4	44.3
0.4	**0.3**	**0.3**	0.0476	326.4	-2327.6	28.6
0.6	**0.2**	**0.2**	0.0294	239.6	-2076.4	28.6
0.8	**0.1**	**0.1**	0.0164	138.7	-1418.7	27.0
0.9	**0.05**	**0.05**	0.3282	2754.6	1793.3	22.4

Table 5-3. π = 15 mN·m^{-1}

x_{CCM}	x_{CHOL}	x_{DPPC}	A^E(nm^2·molecule^{-1})	$\Delta G_M{}^E$ (J·mol^{-1})	ΔG_M (J·mol^{-1})	*Ks* (mN·m^{-1})
0	**0.5**	**0.5**	-0.0281	-384.6	-2073.9	118.0
0.2	**0.4**	**0.4**	0.0022	-69.8	-2640.9	55.1
0.33	**0.33**	**0.33**	0.0415	505.2	-2172.4	38.8
0.4	**0.3**	**0.3**	0.0044	361.7	-2292.2	30.3
0.6	**0.2**	**0.2**	0.0075	254.6	-2061.5	36.1
0.8	**0.1**	**0.1**	0.0033	154.1	-1403.4	31.2
0.9	**0.05**	**0.05**	0.2370	3587.4	2626.2	16.4

Table 5-4. π = 20 mN·m^{-1}

x_{CCM}	x_{CHOL}	x_{DPPC}	A^E(nm^2·molecule^{-1})	ΔG_M^E (J·mol^{-1})	ΔG_M (J·mol^{-1})	Ks (mN·m^{-1})
0	**0.5**	**0.5**	-0.0281	-476.0	-2176.9	162.8
0.2	**0.4**	**0.4**	-0.0146	-38.6	-2627.3	75.7
0.33	**0.33**	**0.33**	0.0175	593.9	-2101.9	61.0
0.4	**0.3**	**0.3**	-0.0143	395.2	-2276.9	98.3
0.6	**0.2**	**0.2**	-0.0077	278.6	-2053.3	69.5
0.8	**0.1**	**0.1**	-0.0098	158.4	-1409.7	43.4
0.9	**0.05**	**0.05**	0.1560	4181.1	3213.3	19.54

Table 5-5. π = 30 mN·m^{-1}

x_{CCM}	x_{CHOL}	x_{DPPC}	A^E(nm^2·molecule^{-1})	ΔG_M^E (J·mol^{-1})	ΔG_M (J·mol^{-1})	Ks (mN·m^{-1})
0	**0.5**	**0.5**	-0.0322	-565.0	-2265.9	191.5
0.2	**0.4**	**0.4**	-0.0198	-146.2	-2734.8	257.3
0.33	**0.33**	**0.33**	0.0041	675.7	-2020.2	113.1
0.4	**0.3**	**0.3**	-0.0169	306.8	-2365.2	130.0
0.6	**0.2**	**0.2**	-0.0122	214.5	-2117.3	119.0
0.8	**0.1**	**0.1**	-0.0176	73.5	-1494.6	74.8
0.9	**0.05**	**0.05**	0.0636	4788.5	3820.7	27.6

Table 5-6. π = 40 mN·m^{-1}

x_{CCM}	x_{CHOL}	x_{DPPC}	A^E(nm^2·molecule^{-1})	ΔG_M^E (J·mol^{-1})	ΔG_M (J·mol^{-1})	Ks (mN·m^{-1})
0	**0.5**	**0.5**	-0.0336	-729.8	-2430.7	340.4
0.2	**0.4**	**0.4**	-0.0159	-247.2	-2835.8	255.9
0.33	**0.33**	**0.33**	0.0021	710.3	-1985.5	243.6
0.4	**0.3**	**0.3**	-0.0171	185.2	-2486.9	131.0
0.6	**0.2**	**0.2**	-0.0121	120.0	-2211.8	164.4
0.8	**0.1**	**0.1**	-0.0227	-29.2	-1597.3	93.0
0.9	**0.05**	**0.05**	0.0342	5090.4	4122.6	48.0